Computational electrodynamics in material media with constraint-preservation, multidimensional Riemann solvers and sub-cell resolution – Part I, second-order FVTD schemes

Dinshaw S. Balsara [a,*], Allen Taflove [b], Sudip Garain [a], Gino Montecinos [c]

[a] *University of Notre Dame, United States*
[b] *Northwestern University, United States*
[c] *University of Chile, Chile*

ARTICLE INFO

ABSTRACT

While classic finite-difference time-domain (FDTD) solutions of Maxwell's equations have served the computational electrodynamics (CED) community very well, formulations based on Godunov methodology have begun to show advantages. We argue that the formulations presented so far are such that FDTD schemes and Godunov-based schemes each have their own unique advantages. However, there is currently not a single formulation that systematically integrates the strengths of both these major strains of development. While an early glimpse of such a formulation was offered in Balsara et al. [16], that paper focused on electrodynamics in plasma. Here, we present a synthesis that integrates the strengths of both FDTD and Godunov-based schemes into a robust single formulation for CED in material media.

Three advances make this synthesis possible. First, from the FDTD method, we retain (but somewhat modify) a spatial staggering strategy for the primal variables. This provides a beneficial constraint preservation for the electric displacement and magnetic induction vector fields via reconstruction methods that were initially developed in some of the first author's papers for numerical magnetohydrodynamics (MHD). Second, from the Godunov method, we retain the idea of upwinding, except that this idea, too, has to be significantly modified to use the multi-dimensionally upwinded Riemann solvers developed by the first author. Third, we draw upon recent advances in arbitrary derivatives in space and time (ADER) time-stepping by the first author and his colleagues. We use the ADER predictor step to endow our method with sub-cell resolving capabilities so that the method can be stiffly stable and resolve significant sub-cell variation in the material properties within a zone.

Overall, in this paper, we report a new scheme for numerically solving Maxwell's equations in material media, with special attention paid to a second-order-accurate formulation. Several numerical examples are presented to show that the proposed technique works. Because of its sub-cell resolving ability, the new method retains second-order accuracy even when material permeability and permittivity vary by an order-of-magnitude over just one or two zones. Furthermore, because the new method is also unconditionally stable in the presence of stiff source terms (i.e., in problems involving giant conductivity variations), it can handle several orders-of-magnitude variation in material conductivity over just one

or two zones without any reduction of the time–step. Consequently, the CFL depends only on the propagation speed of light in the medium being studied.

1. Introduction

The numerical solution of Maxwell's equations plays an extremely important role in many problems in science and engineering. The finite-difference time-domain (FDTD) method (Yee [57], Taflove [47], Taflove and Hagness [48,50], Taflove, Oskooi and Johnson [49]) has been a primary technique for this class of computational electrodynamics (CED) applications for more than a quarter century. Indeed, the FDTD method has many desirable features, including a direct interpretation of the two curl-type equations given by Faraday's Law and the generalized Ampere's Law, and a natural satisfaction of the constraint equations given by Gauss's Laws for electric and magnetic charge. This is achieved by a spatial staggering of the electric field and magnetic field components. On a simple Cartesian mesh, every electric field vector component is surrounded by four circulating magnetic field vector components, and every magnetic field vector component is surrounded by four circulating electric field vector components. This compactly staggered arrangement of primal variables is the source of the FDTD method's strength and versatility. This staggering of divergence-free magnetic field variables has proven so popular that many MHD schemes also use a Yee-type arrangement of the field variables (Brecht et al. [22], Evans and Hawley [30], DeVore [25], Dai and Woodward [24], Ryu et al. [41], Balsara and Spicer [1]).

However, Maxwell's equations constitute a hyperbolic system, and powerful general techniques have been developed in the last three-and-a-half decades for the high-accuracy treatment of hyperbolic systems. Such methods go under the rubric of higher-order Godunov techniques that use a zone-centered formulation. Formulations that treat Maxwell's equations with zone-centered variables have been tried (Munz et al. [38], Ismagilov [34], Barbas and Velarde [19], Elkina and Ruhl [29]; and references therein).

Unfortunately, to date, the literature indicates some inability to reconcile the different collocations used in FDTD versus those used in higher-order Godunov methods. This has been an impediment to progress. As a result, FDTD methods have been unable to benefit from advances in higher-order Godunov methodology, and likewise higher-order Godunov methods have been unable to deliver on some of the valuable constraint-preserving properties of FDTD.

The motivation for using higher-order Godunov methodology is quite compelling (Munz et al. [38]). Adaptive mesh refinement (AMR) becomes easy with such methods because they retain a single control volume rather than the linked pair of control volumes used in FDTD schemes. They also offer good phase accuracy and, especially at higher orders, the dissipation is well controlled and restricted to waves that have wavelength comparable to the mesh size. (Such small-scale waves are often the consequence of spurious reflection at mesh refinement boundaries, and Elkina and Ruhl [29] show that such spurious waves are properly controlled by higher-order Godunov schemes.) In the context of CED, such techniques are broadly termed finite-volume time-domain (FVTD) methods. There is another strain of allied work using discontinuous Galerkin schemes (Hesthaven and Warburton [32]). These are termed discontinuous-Galerkin time-domain (DGTD) methods in the context of CED. DGTD methods are attractive because of their ability to handle complex geometry. Importantly, neither the current generation of DGTD methods nor the current generation of FVTD methods automatically preserves constraints for the electric displacement and magnetic induction vector fields.

The goal of this paper is to bridge the divide between FDTD and FVTD methods for CED with a new synthesis. Such a synthesis was initially explored in Balsara et al. [16]. However, that paper focused on CED in plasma. In this paper, we take the synthesis much further by considering material media. It should also be pointed out that Balsara and Kappeli [18] have recently proposed discontinuous Galerkin methods for magnetohydrodynamics (MHD) that are constraint-preserving. As a result, the methods presented here can also be viewed as laying the groundwork for an analogous synthesis between FDTD and DGTD methods in CED.

The methods that we report here are certainly higher-order Godunov in spirit. We use all the same philosophies of higher-order non-oscillatory reconstruction and upwinding via Riemann solvers that have made the higher-order Godunov schemes so popular. But, in addition, we employ a spatial staggering of the field variables that is borrowed – with modifications – from the Yee mesh used in FDTD. Three special advances arise from this synthesis, as follows.

First, we use a special form of constraint-preserving reconstruction. Some aspects of this reconstruction have been developed in the literature for MHD simulations (Balsara [2–4], Balsara and Dumbser [12], Xu et al. [58], Balsara et al. [16]), but importing these ideas to CED is genuinely novel.

Second, we draw on recently developed multidimensional Riemann solver technology (Balsara [7,8,11,14], Balsara, Dumbser and Abgrall [10], Balsara and Dumbser [13], Balsara et al. [15]). This enables us to get the correct multidimensionally upwinded update of Maxwell's equations on a Yee-adapted mesh.

Third, we implement a fundamental advance in time-stepping. A CED code must accurately account for substantial variations in material properties (permittivity, permeability, and conductivity) that occur within only one or two zones, including abrupt changes at material interfaces and conductor surfaces. To robustly model these variations, we incorporate a novel Arbitrary DERivatives in space and time (ADER) scheme for stiff source terms. This scheme acts on nodal points within a zone. Because the values of the material properties and their gradients are allowed to vary substantially at each of the nodal

points within a zone, we can incorporate sub-cell variations in these properties into our time-stepping strategy. The source terms associated with the current are also treated stiffly, permitting an A-stable, sub-cell-resolving time-update strategy. This advance has many potential uses for adaptive mesh refinement-based treatment of CED, especially because the trend in such simulations is to simulate geometrically complex material structures on Cartesian meshes with local refinement at the boundaries of these structures (Zakharian et al. [59], Elkina and Ruhl [29]).

In this paper (the first of a planned series), we apply our proposed synthesis to implement second-order schemes for CED in material media. This focus allows us to pay special attention to the hyperbolic nature of the problem and study the eigensystem in great detail. We present the constraint-preserving reconstruction in its simplest form at the second order of accuracy. The ADER scheme is likewise simplified, but it is also tailored to meet the unique design goals of CED. The multidimensional Riemann solver for CED is discussed in depth. In a subsequent paper, we will show how these ideas extend to higher orders of accuracy. The eigensystem does not get modified at higher orders, nor does the Riemann solver. Therefore, in the sequel paper, we will focus on the design of constraint-preserving reconstruction at higher orders. In the sequel paper, we will also focus on ADER schemes at higher order that are tailored to meet the design goals of CED at higher order.

This paper is the first time that a confluence of new techniques have been brought together for CED in such a way that all the advantages of FDTD are preserved within the context of Godunov schemes. The application of higher order Godunov methodology to CED provides multiple advantages: 1) The method retains accuracy even when there are order of magnitude variations in dielectric properties. 2) The method suffers no degradation in CFL even when there are large variations in conductivity. 3) The method can accommodate to situations where the material properties depend on the electric and magnetic fields. In a sequel paper, we show that these three advantages extend seamlessly to higher orders of accuracy. 4) The method uses only one control volume and can take well to adaptive mesh refinement, as we will show in another subsequent paper. There are other areas where seemingly linear problems are being solved, like aeroacoustics and linear elasticity. In such areas too, higher order Godunov schemes have shown themselves to be beneficial, and we hope that this sequence of papers illustrates the benefits for CED.

Section 2 of this paper documents the equations of CED, and studies the eigensystem for Maxwell's equations in material media with general permittivity and permeability tensors. Section 3 briefly describes constraint-preserving reconstruction for CED at second order. Section 4 presents a very special ADER scheme that is well-suited to the needs of CED at second order. Section 5 documents the multidimensional Riemann solver for CED. Section 6 presents a pointwise synopsis of the numerical method at second order. Section 7 presents illustrative results, and Section 8 provides the conclusions.

2. Equations of CED in material media and an analysis of the eigenstructure

Sub-section 2.1 explains the equation structure of the equations of CED. Sub-section 2.2 analyzes the eigenstructure of the resulting hyperbolic system in the simple, but very useful, case where the permittivity and permeability tensors are diagonal. Sub-section 2.3 extends the same analysis to permittivity and permeability tensors that have off-diagonal terms. Sub-section 2.4 quickly analyzes the computational tasks that are needed for the numerical solution of the system of equations in Sub-section 2.1. This provides a roadmap for the later sections. We, therefore, advise the first-time reader to read Sub-section 2.4 even if s/he should feel like skipping Sub-sections 2.2 and 2.3.

2.1. The equations of CED

The equations of CED can be written as two evolutionary curl-type equations for the magnetic induction and the electric displacement. The first of these is Faraday's law given by

$$\frac{\partial \mathbf{B}}{\partial t} + \nabla \times \mathbf{E} = -\mathbf{M} \tag{2.1}$$

where $\mathbf{B}$ is the magnetic induction (or magnetic flux density), $\mathbf{E}$ is the electric field and $\mathbf{M}$ is the magnetic current density. For CED, it is best to take the magnetic current density to be non-zero. The reason for this choice is that the magnetic current density may need to be non-zero in order to impose boundary conditions; even though physically-speaking it is always zero in any material because of the absence of magnetic monopoles. The second evolutionary equation for the electric displacement is the extended Ampere's law given by

$$\frac{\partial \mathbf{D}}{\partial t} - \nabla \times \mathbf{H} = -\mathbf{J} \tag{2.2}$$

where $\mathbf{D}$ is the electric displacement (or electric flux density), $\mathbf{H}$ is the magnetic field vector and $\mathbf{J}$ is the electric current density. The magnetic induction and the electric displacement also satisfy the following two non-evolutionary constraint equations given by

$$\nabla \cdot \mathbf{B} = \rho_M \tag{2.3}$$

and

$$\nabla \cdot \mathbf{D} = \rho_E \tag{2.4}$$

where ρ_M and ρ_E are the magnetic and electric charge densities. In any physical medium $\rho_M = 0$; however, the imposition of PML boundary conditions (Berenger [20,21], Katz, Thiel and Taflove [36], Taflove and Hagness [48]) might require the use of non-zero magnetic current densities.

With the above equations, it is easy to show the following continuity equations for the electric charge

$$\frac{\partial \rho_E}{\partial t} + \nabla \cdot \mathbf{J} = 0 \tag{2.5}$$

and the magnetic charge

$$\frac{\partial \rho_M}{\partial t} + \nabla \cdot \mathbf{M} = 0 \tag{2.6}$$

In material media, the electric displacement vector is also related to the electric field vector via a constitutive relation given by

$$\mathbf{D} = \boldsymbol{\varepsilon} \mathbf{E} \tag{2.7}$$

where, in general, $\boldsymbol{\varepsilon}$ is a symmetric 3×3 permittivity tensor that depends on material properties. Likewise, in material media, the magnetic induction vector is related to the magnetic field vector by

$$\mathbf{B} = \boldsymbol{\mu} \mathbf{H} \tag{2.8}$$

As before, $\boldsymbol{\mu}$ is a symmetric 3×3 magnetic permeability tensor that depends on material properties. We allow the permittivity and magnetic permeability tensors to have a general form. However, the analytical eigenstructure of the hyperbolic system is most easily found by making the simplifying assumption $\boldsymbol{\varepsilon} = \text{diag}\{\varepsilon_{xx}, \varepsilon_{yy}, \varepsilon_{zz}\}$ and $\boldsymbol{\mu} = \text{diag}\{\mu_{xx}, \mu_{yy}, \mu_{zz}\}$. We will also need the inverses of the permittivity and permeability tensors. These 3×3 inverse matrices will also be symmetric and we denote them as $\tilde{\boldsymbol{\varepsilon}} \equiv \boldsymbol{\varepsilon}^{-1}$ and $\tilde{\boldsymbol{\mu}} \equiv \boldsymbol{\mu}^{-1}$. The current density is related to the electric field via

$$\mathbf{J} = \sigma \mathbf{E} \tag{2.9}$$

where σ is the conductivity. Similarly, the magnetic current density is related to the magnetic field via

$$\mathbf{M} = \sigma^* \mathbf{H} \tag{2.10}$$

where σ^* is the equivalent magnetic loss, which is again zero in physical media, but may be non-zero when imposing boundary conditions in CED.

The CED equations can be written in a flux form, which we formally write as

$$\partial_t \mathbf{U} + \partial_x \mathbf{F} + \partial_y \mathbf{G} + \partial_z \mathbf{K} = \mathbf{S} \tag{2.11}$$

Here $\mathbf{U}$ is the vector of conserved variables, $\mathbf{F}$, $\mathbf{G}$ and $\mathbf{K}$ are flux vectors in the x-, y- and z-directions, and $\mathbf{S}$ is the vector of source terms. In general, the source terms can be stiff in a high-conductivity medium, so the numerical method has to accommodate for stiff source terms. We wish to directly impose the constraints (2.3) and (2.4) on the same finite volume because this opens the door to the use of powerful methods from higher-order Godunov schemes, and it also helps out with adaptive mesh refinement. As a result, we take our magnetic induction and electric displacement vectors as the primal variables. The normal components of these two vector fields are indeed our primal variables and are defined at the faces of the control volume, as shown in Fig. 1. Notice, that this too will lead to a pair of Yee-type curl equations as long as the electric and magnetic fields can be specified in some multidimensionally upwinded sense at the edges of the mesh. We will describe how this is done in a subsequent section. Let us now explicitly specify the vector of conserved variables $\mathbf{U}$, the fluxes $\mathbf{F}$, $\mathbf{G}$ and $\mathbf{K}$, and the source term $\mathbf{S}$ below

$$\mathbf{U} = \begin{pmatrix} D_x \\ D_y \\ D_z \\ B_x \\ B_y \\ B_z \end{pmatrix}; \quad \mathbf{F} = \begin{pmatrix} 0 \\ \tilde{\mu}_{xz}B_x + \tilde{\mu}_{yz}B_y + \tilde{\mu}_{zz}B_z \\ -\tilde{\mu}_{xy}B_x - \tilde{\mu}_{yy}B_y - \tilde{\mu}_{yz}B_z \\ 0 \\ -\tilde{\varepsilon}_{xz}D_x - \tilde{\varepsilon}_{yz}D_y - \tilde{\varepsilon}_{zz}D_z \\ \tilde{\varepsilon}_{xy}D_x + \tilde{\varepsilon}_{yy}D_y + \tilde{\varepsilon}_{yz}D_z \end{pmatrix}; \quad \mathbf{G} = \begin{pmatrix} -\tilde{\mu}_{xz}B_x - \tilde{\mu}_{yz}B_y - \tilde{\mu}_{zz}B_z \\ 0 \\ \tilde{\mu}_{xx}B_x + \tilde{\mu}_{xy}B_y + \tilde{\mu}_{xz}B_z \\ \tilde{\varepsilon}_{xz}D_x + \tilde{\varepsilon}_{yz}D_y + \tilde{\varepsilon}_{zz}D_z \\ 0 \\ -\tilde{\varepsilon}_{xx}D_x - \tilde{\varepsilon}_{xy}D_y - \tilde{\varepsilon}_{xz}D_z \end{pmatrix};$$

$$\mathbf{K} = \begin{pmatrix} \tilde{\mu}_{xy}B_x + \tilde{\mu}_{yy}B_y + \tilde{\mu}_{yz}B_z \\ -\tilde{\mu}_{xx}B_x - \tilde{\mu}_{xy}B_y - \tilde{\mu}_{xz}B_z \\ 0 \\ -\tilde{\varepsilon}_{xy}D_x - \tilde{\varepsilon}_{yy}D_y - \tilde{\varepsilon}_{yz}D_z \\ \tilde{\varepsilon}_{xx}D_x + \tilde{\varepsilon}_{xy}D_y + \tilde{\varepsilon}_{xz}D_z \\ 0 \end{pmatrix}; \quad \mathbf{S} = \begin{pmatrix} -\sigma(\tilde{\varepsilon}_{xx}D_x + \tilde{\varepsilon}_{xy}D_y + \tilde{\varepsilon}_{xz}D_z) \\ -\sigma(\tilde{\varepsilon}_{xy}D_x + \tilde{\varepsilon}_{yy}D_y + \tilde{\varepsilon}_{yz}D_z) \\ -\sigma(\tilde{\varepsilon}_{xz}D_x + \tilde{\varepsilon}_{yz}D_y + \tilde{\varepsilon}_{zz}D_z) \\ -\sigma^*(\tilde{\mu}_{xx}B_x + \tilde{\mu}_{xy}B_y + \tilde{\mu}_{xz}B_z) \\ -\sigma^*(\tilde{\mu}_{xy}B_x + \tilde{\mu}_{yy}B_y + \tilde{\mu}_{yz}B_z) \\ -\sigma^*(\tilde{\mu}_{xz}B_x + \tilde{\mu}_{yz}B_y + \tilde{\mu}_{zz}B_z) \end{pmatrix} \tag{2.12}$$

It is important to write the fluxes in the above format explicitly because that is the form in which they will contribute to the characteristic analysis in the next two sub-sections. The characteristic analysis of wave speeds plays a central role in the design of higher-order Godunov schemes. Similarly, the explicit form of the source terms is needed because we will show in a later section how the source terms are implicitly evolved in time within each zone. This will be done in a fashion where the source terms stay coupled to the space–time evolution of the vector of conserved variables; so that the stiffness in the source terms is respected.
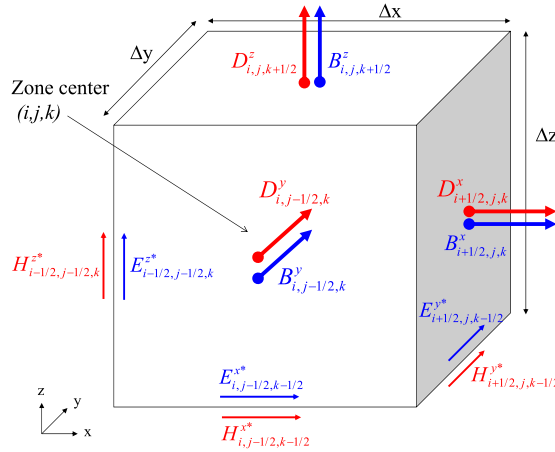
Fig. 1. The figure shows us that the primal variables of the scheme, given by the normal components of the magnetic induction and electric field displacement, are facially-collocated. They undergo an update from Faraday's law and the generalized Ampere's law respectively. The components of the primal magnetic induction vector are shown by the thick blue arrows while the components of the primal electric displacement vector are shown by the thick red arrows. The edge-collocated electric fields, which are used for updating the facial magnetic induction components, are shown by the thin blue arrows close to the appropriate edge. The edge-collocated magnetic fields, which are used for updating the facial electric displacement components, are shown by the thin red arrows close to the appropriate edge. (For interpretation of the references to color in this figure legend, the reader is referred to the web version of this article.)

2.2. Eigenstructure for diagonal permittivity and permeability matrices

When the permittivity and permeability matrices are diagonal, which is the usual case in CED, we can write out the eigenvalues and eigenvectors of the characteristic matrices explicitly. To keep this sub-section short, the corresponding eigenvectors have been catalogued in Appendix A. Please note that the diagonal permittivity and permeability matrices do not need to have the same value for all their diagonal terms. We will need the eigenvalues for wave propagation in the x- and y-directions in order to design the multidimensional Riemann solver that yields the z-components of the electric and magnetic fields at the z-edges of the mesh; see Fig. 1. For that reason, in this sub-section we provide the eigenvalues in both the x- and y-directions.

The characteristic matrix $\partial \mathbf{F}/\partial \mathbf{U}$ enables the propagation of x-directional waves with the following diagonal matrix of eigenvalues

$$\mathbf{\Lambda}^x = \text{diag}\left(-\sqrt{\tilde{\varepsilon}_{yy}\tilde{\mu}_{zz}}, \quad -\sqrt{\tilde{\varepsilon}_{zz}\tilde{\mu}_{yy}}, \quad 0, \quad 0, \quad \sqrt{\tilde{\varepsilon}_{zz}\tilde{\mu}_{yy}}, \quad \sqrt{\tilde{\varepsilon}_{yy}\tilde{\mu}_{zz}} \right) \tag{2.13}$$

The corresponding eigenvectors of eqn. (2.13) are catalogued in Appendix A.

The characteristic matrix $\partial \mathbf{G}/\partial \mathbf{U}$ enables the propagation of y-directional waves with the following diagonal matrix of eigenvalues

$$\mathbf{\Lambda}^y = \text{diag}\left(-\sqrt{\tilde{\varepsilon}_{xx}\tilde{\mu}_{zz}}, \quad -\sqrt{\tilde{\varepsilon}_{zz}\tilde{\mu}_{xx}}, \quad 0, \quad 0, \quad \sqrt{\tilde{\varepsilon}_{zz}\tilde{\mu}_{xx}}, \quad \sqrt{\tilde{\varepsilon}_{xx}\tilde{\mu}_{zz}} \right) \tag{2.14}$$

The corresponding eigenvectors of eqn. (2.14) are catalogued in Appendix A.

Please note that we may have situations where $\tilde{\varepsilon}_{zz}\tilde{\mu}_{yy} > \tilde{\varepsilon}_{yy}\tilde{\mu}_{zz}$; as a result, we cannot guarantee that the eigenvalues in eqn. (2.13) form an ordered set. But that is immaterial in practical computation because we can indeed guarantee that the eigenvectors in Appendix A provide a complete set of orthonormal eigenvectors. Similarly, we may have situations where $\tilde{\varepsilon}_{zz}\tilde{\mu}_{xx} > \tilde{\varepsilon}_{xx}\tilde{\mu}_{zz}$; as a result, we cannot guarantee that the eigenvalues in eqn. (2.14) form an ordered set. As before, this is immaterial in practical computation.

2.3. Eigenstructure for permittivity and permeability matrices with non-diagonal terms

In some instances, especially when dealing with the interface between two materials with different dielectric properties, it is very useful to be able to treat the situation where the permittivity and permeability tensors have non-diagonal terms (Farjadpour et al. [31], Oskooi et al. [39], Taflove, Oskooi, and Johnson [49]). This is usually needed at dielectric interfaces. In order to design a multidimensional Riemann solver for such situations, it is very useful to be able to evaluate the eigenstructure when the permittivity and permeability tensors have non-diagonal terms. In this sub-section, we present all the details for obtaining the eigenstructure for non-diagonal permittivity and permeability tensors. The eigenvalues that we catalogue are such that they will smoothly retrieve eqns. (2.13) and (2.14) in the limit where these tensors become diagonal tensors.

It is important to realize that when the tensors for the material properties are non-diagonal, the eigenvalues will be disjoint. Thus each of the eigenvectors that we pick will be orthogonal to the other eigenvectors. In practice, it is always

profitable to check whether the permittivity and permeability tensors are diagonal. If they are diagonal, please use the easy-to-evaluate expressions from the previous sub-section and Appendix A. If they are not diagonal, then and then only do we recommend using the expressions from this sub-section and Appendix B. In fact, the eigenvectors (though not the eigenvalues) can attain an indeterminate (zero divided by zero) form if one makes a naïve use of the formulae in this section when the permittivity and permeability become diagonal tensors. The structure of the eigenvectors has no impact on practical computations in the algorithm presented here.

Now, the characteristic matrix $\partial \mathbf{F}/\partial \mathbf{U}$ enables the propagation of x-directional waves with the following diagonal matrix of eigenvalues

$$\mathbf{\Lambda}^x = \mathrm{diag}\left(-\sqrt{\tau^x + \chi^x \sqrt{\kappa^x}}/\sqrt{2}, \quad -\sqrt{\tau^x - \chi^x \sqrt{\kappa^x}}/\sqrt{2}, \quad 0, \quad 0, \quad \sqrt{\tau^x - \chi^x \sqrt{\kappa^x}}/\sqrt{2}, \quad \sqrt{\tau^x + \chi^x \sqrt{\kappa^x}}/\sqrt{2} \right)$$

$$\text{with} \quad \tau^x = \tilde{\varepsilon}_{yy}\tilde{\mu}_{zz} + \tilde{\varepsilon}_{zz}\tilde{\mu}_{yy} - 2\tilde{\varepsilon}_{yz}\tilde{\mu}_{yz}$$

$$\text{and} \quad \kappa^x = (\tilde{\varepsilon}_{yy}\tilde{\mu}_{zz} - \tilde{\varepsilon}_{zz}\tilde{\mu}_{yy})^2 + 4(\tilde{\varepsilon}_{yy}\tilde{\mu}_{yz} - \tilde{\varepsilon}_{yz}\tilde{\mu}_{yy})(\tilde{\varepsilon}_{zz}\tilde{\mu}_{yz} - \tilde{\varepsilon}_{yz}\tilde{\mu}_{zz})$$

$$\text{and} \quad \chi^x = \mathrm{sgn}(\tilde{\varepsilon}_{yy}\tilde{\mu}_{zz} - \tilde{\varepsilon}_{zz}\tilde{\mu}_{yy}) \tag{2.15}$$

The eigenvalues in eqn. (2.15) are so designed that we smoothly retrieve the limit in eqn. (2.13) when the permittivity and permeability become diagonal tensors. The corresponding eigenvectors of eqn. (2.15) are catalogued in Appendix B.

The characteristic matrix $\partial \mathbf{G}/\partial \mathbf{U}$ enables the propagation of y-directional waves with the following diagonal matrix of eigenvalues

$$\mathbf{\Lambda}^y = \mathrm{diag}\left(-\sqrt{\tau^y + \chi^y \sqrt{\kappa^y}}/\sqrt{2}, \quad -\sqrt{\tau^y - \chi^y \sqrt{\kappa^y}}/\sqrt{2}, \quad 0, \quad 0, \quad \sqrt{\tau^y - \chi^y \sqrt{\kappa^y}}/\sqrt{2}, \quad \sqrt{\tau^y + \chi^y \sqrt{\kappa^y}}/\sqrt{2} \right)$$

$$\text{with} \quad \tau^y = \tilde{\varepsilon}_{xx}\tilde{\mu}_{zz} + \tilde{\varepsilon}_{zz}\tilde{\mu}_{xx} - 2\tilde{\varepsilon}_{xz}\tilde{\mu}_{xz}$$

$$\text{and} \quad \kappa^y = (\tilde{\varepsilon}_{xx}\tilde{\mu}_{zz} - \tilde{\varepsilon}_{zz}\tilde{\mu}_{xx})^2 + 4(\tilde{\varepsilon}_{xx}\tilde{\mu}_{xz} - \tilde{\varepsilon}_{xz}\tilde{\mu}_{xx})(\tilde{\varepsilon}_{zz}\tilde{\mu}_{xz} - \tilde{\varepsilon}_{xz}\tilde{\mu}_{zz})$$

$$\text{and} \quad \chi^y = \mathrm{sgn}(\tilde{\varepsilon}_{xx}\tilde{\mu}_{zz} - \tilde{\varepsilon}_{zz}\tilde{\mu}_{xx}) \tag{2.16}$$

The eigenvalues in eqn. (2.16) are so designed that we smoothly retrieve the limit in eqn. (2.14) when the permittivity and permeability become diagonal tensors. The corresponding eigenvectors of eqn. (2.16) are catalogued in Appendix B, which will be made available to the reader via the web-based supplemental parts of this paper.

2.4. Computational tasks needed for constraint-preserving Godunov schemes for CED

Let us take Fig. 1 as our starting point. The facially-collocated normal components of the electric displacement and the magnetic induction constitute the primal variables of our scheme. These are shown by the thick red arrow and the thick blue arrow respectively in each of the faces of the cuboidal element shown in Fig. 1. In a finite-volume sense, these primal variables are actually taken to be facial averages of the normal components of the electric displacement and the magnetic induction. The overall task consists of finding the edge-collocated components of the magnetic field vector and the electric field vector shown in Fig. 1. These are shown with the thinner red arrow and the thinner blue arrow respectively next to the edges of the zone shown in Fig. 1. In a finite-volume sense, these are actually averages in one space dimension (taken to be the length of the element's edge) and the time dimension (evaluated over the timestep). In the spirit of a Godunov scheme, these edge-collocated variables have to be properly upwinded. Recall though that for a conservation law, the upwinding of the facial fluxes can be one-dimensional; and in a Godunov scheme this is accomplished with a one-dimensional Riemann solver. However, eqns. (2.1) and (2.2) call for curl-type updates. Consequently, these edge-collocated variables (which reside in the edges of the mesh) should be upwinded by a method that can smoothly accommodate upwinding in both the directions that are transverse to the edge in question. In other words, we need at least a two-dimensional Riemann solver. If these space–time averaged components of the magnetic field vector and the electric field vector are available at the edges of the mesh, a single step update for the entire set of CED equations, consistent with eqns. (2.1) and (2.2) can be written as

$$\bar{\mathrm{D}}_{x;i+1/2,j,k}^{n+1} = \bar{\mathrm{D}}_{x;i+1/2,j,k}^{n} - \bar{\mathrm{J}}_{x;i+1/2,j,k}\Delta t$$
$$+ \frac{\Delta t}{\Delta y \Delta z}(\Delta z \bar{\mathrm{H}}_{z;i+1/2,j+1/2,k} - \Delta z \bar{\mathrm{H}}_{z;i+1/2,j-1/2,k} + \Delta y \bar{\mathrm{H}}_{y;i+1/2,j,k-1/2} - \Delta y \bar{\mathrm{H}}_{y;i+1/2,j,k+1/2})$$

$$\tag{2.17a}$$

$$\bar{\mathrm{D}}_{y;i,j-1/2,k}^{n+1} = \bar{\mathrm{D}}_{y;i,j-1/2,k}^{n} - \bar{\mathrm{J}}_{y;i,j-1/2,k}\Delta t$$
$$+ \frac{\Delta t}{\Delta x \Delta z}(\Delta x \bar{\mathrm{H}}_{x;i,j-1/2,k+1/2} - \Delta x \bar{\mathrm{H}}_{x;i,j-1/2,k-1/2} + \Delta z \bar{\mathrm{H}}_{z;i-1/2,j-1/2,k} - \Delta z \bar{\mathrm{H}}_{z;i+1/2,j-1/2,k})$$

$$\tag{2.17b}$$

$$\bar{D}_{z;i,j,k+1/2}^{n+1} = \bar{D}_{z;i,j,k+1/2}^{n} - \bar{J}_{z;i,j,k+1/2}\Delta t$$
$$+ \frac{\Delta t}{\Delta x \Delta y}(\Delta x \bar{H}_{x;i,j-1/2,k+1/2} - \Delta x \bar{H}_{x;i,j+1/2,k+1/2} + \Delta y \bar{H}_{y;i+1/2,j,k+1/2} - \Delta y \bar{H}_{y;i-1/2,j,k+1/2})$$

$$(2.17c)$$

and

$$\bar{B}_{x;i+1/2,j,k}^{n+1} = \bar{B}_{x;i+1/2,j,k}^{n} - \bar{M}_{x;i+1/2,j,k}\Delta t$$
$$- \frac{\Delta t}{\Delta y \Delta z}(\Delta z \bar{E}_{z;i+1/2,j+1/2,k} - \Delta z \bar{E}_{z;i+1/2,j-1/2,k} + \Delta y \bar{E}_{y;i+1/2,j,k-1/2} - \Delta y \bar{E}_{y;i+1/2,j,k+1/2}) \quad (2.18a)$$

$$\bar{B}_{y;i,j-1/2,k}^{n+1} = \bar{B}_{y;i,j-1/2,k}^{n} - \bar{M}_{y;i,j-1/2,k}\Delta t$$
$$- \frac{\Delta t}{\Delta x \Delta z}(\Delta x \bar{E}_{x;i,j-1/2,k+1/2} - \Delta x \bar{E}_{x;i,j-1/2,k-1/2} + \Delta z \bar{E}_{z;i-1/2,j-1/2,k} - \Delta z \bar{E}_{z;i+1/2,j-1/2,k}) \quad (2.18b)$$

$$\bar{B}_{z;i,j,k+1/2}^{n+1} = \bar{B}_{z;i,j,k+1/2}^{n} - \bar{M}_{z;i,j,k+1/2}\Delta t$$
$$- \frac{\Delta t}{\Delta x \Delta y}(\Delta x \bar{E}_{x;i,j-1/2,k+1/2} - \Delta x \bar{E}_{x;i,j+1/2,k+1/2} + \Delta y \bar{E}_{y;i+1/2,j,k+1/2} - \Delta y \bar{E}_{y;i-1/2,j,k+1/2}) \quad (2.18c)$$

We also have to pay attention, of course, to the source terms for the electric current density and the magnetic current density on the right hand sides of eqns. (2.1) and (2.2). In certain instances, when the conduction becomes substantial, these source terms can become stiff.

With this preview, we are now ready to decompose the computational tasks. Since the primal variables are facially-averaged normal components of the electric displacement and magnetic induction, we need to endow these components with sub-structure. In doing so, we follow the philosophy of van Leer [55,56]. Thus, by locating ourselves at a face and using the adjacent faces that are von Neumann neighbors of that face, we can carry out a second-order or higher-order total variation diminishing (TVD) or weighted essentially non-oscillatory (WENO) reconstruction within that face. For instance, at second order of accuracy, the x-component of the magnetic induction will have linear sub-structure in the y- and z-directions. This gives us linear sub-structure within each face. However, from eqn. (2.11) realize that if we want to make a space–time extension of a partial differential equation (PDE), we necessarily need all its derivatives within a control volume. The vector fields in question – i.e. the electric displacement and the magnetic induction – satisfy constraint equations; please see eqns. (2.3) and (2.4). Thus, the volumetric reconstruction of these vector fields within the control volume shown in Fig. 1 should be made consistent with the constraint equations. It should also be made consistent with the linear (or higher order) profiles that we have endowed to the components within each face. A mathematically tight way of carrying out the constraint-preserving reconstruction that respects all the physics is presented in Section 3.

Once the reconstruction from the previous paragraph is done, we will have the spatial variation of the electric displacement vector field and the magnetic induction vector field at all locations within all the control volumes (elements) that make up the mesh. It is still not possible to obtain the one-step update that we seek in eqns. (2.16) and (2.18). To obtain such a one-step update, we need time-centered and time-averaged magnetic fields and electric fields. As a result, we need an approach that time-evolves the PDE system in-the-small within each zone. A general approach for doing this is given by the ADER scheme. However, notice that we would like to have two further special requirements in CED. First, the permittivity and permeability tensors can have substantial variation at dielectric interfaces (Farjadpour et al. [31], Oskooi et al. [39], Taflove, Oskooi, and Johnson [49]). Indeed, that variation can be specified within each zone and from eqn. (2.12) we see that the fluxes should account for such variation. Second, the source terms can be stiff and can also have substantial variation within a zone; see eqns. (2.9) and (2.10). This can happen when the conduction is high or when we are dealing with a perfectly matched layer (PML) boundary condition (Berenger [20,21], Katz, Thiel and Taflove [36], Taflove and Hagness [48]). The source terms can also become stiff when a CED calculation is coupled to another calculation, like a multi-level atom lasing calculation (Chang and Taflove [23]). Thus, the in-the-small update method should account for stiffness that can be spatially varying. For all of these reasons, we design a special type of ADER scheme at second order in Section 4. This ADER scheme is referred to as the ADER predictor step since it predicts an in-the-small evolution for the PDE within each zone/element. The higher-order extension of this ADER scheme will be presented in a sequel paper.

With the ADER step applied, as described in the previous paragraph, we will have an in-the-small space–time evolution of the entire PDE system within each zone/element that makes up the mesh. True to the spirit of a higher-order Godunov scheme, the neighboring elements need to interact in a multidimensionally upwinded sense. This is accomplished at each edge of the mesh with the multidimensional Riemann solver described in Section 5. The multidimensional Riemann solver gives us the properly upwinded components of the magnetic field and the electric field within each edge. Because of our use of the ADER predictor step, these components of the magnetic field and the electric field within each edge will also be properly space-averaged and time-averaged. These are exactly the components that we need in the update eqns. (2.16) and (2.18). This step where the Riemann solver is applied is also called the corrector step, because it gives us the edge-centered terms that are needed for the final update.

The ADER scheme also gives, as a bonus, a space–time evolution of the source terms within each zone. Since these source terms have been time-evolved in a fashion that accounts for any possible stiffness, we can also obtain the facially and temporally averaged source terms in eqns. (2.16) and (2.18). The time-averaging is done over each timestep. These can be obtained within each face by averaging from the zones that abut the face. This gives us the requisite source terms within each face.

The previous two paragraphs have shown us that all the variables that are needed for the update in eqns. (2.16) and (2.18) are in hand. The update can, therefore, be carried out. For the scheme described in this paper, it yields a second-order-accurate update in space and time. However, the entire procedure can be extended to higher orders, as we will show in a sequel paper.

3. Constraint-preserving reconstruction with second order accuracy for CED

Many of the ideas described here were originally developed in Balsara [2–4] and Balsara and Dumbser [12] and Xu et al. [58]. These ideas were initially developed within the context of divergence-free MHD schemes; but they change quite a bit when applied to CED. Notice from eqn. (2.4) that the displacement vector is not divergence-free. The primal variables of our scheme are facially-averaged normal components of the electric displacement and magnetic induction. Given the congruence between eqns. (2.3) and (2.4), we find it more advantageous to develop a constraint-preserving high-order strategy for reconstructing the displacement vector at all locations within the zone shown in Fig. 1. This is needed for the ADER scheme in Section 4 which looks at the entire PDE in eqns. (2.11) and (2.12) as a whole and tries to evolve the initial data in-the-small as a function of time. It is also needed because we need to give our best reconstructed and predicted values for the electric displacement and magnetic induction as inputs to the multidimensional Riemann solver described in Section 5.

With the normal components of the electric displacement specified at each face of the mesh, the zone-averaged electric charge density can be obtained for each zone. This is done by the application of a divergence operator to the facially-collocated normal components of the electric displacement vector. Let $\bar{D}_0^{x+}$ and $\bar{D}_0^{x-}$ be the facially-averaged x-components of the electric displacement vector collocated at the top and bottom x-faces of the zone shown in Fig. 1. Similarly, let $\bar{D}_0^{y+}$ and $\bar{D}_0^{y-}$ be the facially-averaged y-components of the electric displacement vector collocated at the top and bottom y-faces of the zone shown in Fig. 1. Likewise, let $\bar{D}_0^{z+}$ and $\bar{D}_0^{z-}$ be the facially-averaged z-components of the electric displacement vector collocated at the top and bottom z-faces of the zone shown in Fig. 1. For a cuboidal zone with zone sizes Δx, Δy and Δz in the three directions, we can evaluate the mean electric charge density within the zone as

$$\bar{\rho}_{E;0} = \frac{\bar{D}_0^{x+} - \bar{D}_0^{x-}}{\Delta x} + \frac{\bar{D}_0^{y+} - \bar{D}_0^{y-}}{\Delta y} + \frac{\bar{D}_0^{z+} - \bar{D}_0^{z-}}{\Delta z} \tag{3.1}$$

Once this zone-averaged electric charge density is obtained within each zone, we can use standard zone-centered TVD or WENO reconstruction methods to reconstruct the charge density to the desired order. For basics on WENO reconstruction, please see Jiang and Shu [35], Balsara and Shu [5], Dumbser and Käser [26] and Balsara, Garain and Shu [17]. For second order, the reconstructed electric charge density is given by

$$\rho_{E;0}(x, y, z) = \bar{\rho}_{E;0} + \frac{\Delta_x \rho_{E;0}}{\Delta x} x + \frac{\Delta_y \rho_{E;0}}{\Delta y} y + \frac{\Delta_z \rho_{E;0}}{\Delta z} z \tag{3.2}$$

The coordinates in this Section are measured relative to the zone-center. The vector field for the electric displacement within the zone shown in Fig. 1 will have to be reconstructed so that it is consistent, up to the desired order of accuracy, with the constraint equation

$$\partial_x D^x(x, y, z) + \partial_y D^y(x, y, z) + \partial_z D^z(x, y, z) = \rho_{E;0}(x, y, z) \tag{3.3}$$

The above equation is not the only equation that determines the electric displacement vector field, as we shall see in the next paragraph.

Just as we added sub-structure to the electric charge density in eqn. (3.2), we also wish to add sub-structure to the normal component of the electric displacement vector within each face. At each face, this can be done in a TVD or WENO sense by looking at the adjacent faces and reconstructing the facial component to the desired order of accuracy. At second order, the x-component of the electric displacement within the top and bottom x-faces is given by

$$D^{x+}(y, z) = \bar{D}_0^{x+} + \frac{\Delta_y D_0^{x+}}{\Delta y} y + \frac{\Delta_z D_0^{x+}}{\Delta z} z; \qquad D^{x-}(y, z) = \bar{D}_0^{x-} + \frac{\Delta_y D_0^{x-}}{\Delta y} y + \frac{\Delta_z D_0^{x-}}{\Delta z} z \tag{3.4}$$

To take an example, $\Delta_y D_0^{x+}$ can be obtained by looking at the neighboring x-faces in the y-direction and using their stored facial values to obtain a TVD- or WENO-limited undivided difference. Similarly, $\Delta_z D_0^{x+}$ can be obtained by looking at the neighboring x-faces in the z-direction and using their stored facial values to obtain a TVD- or WENO-limited undivided difference. In an analogous fashion, the y-component of the electric displacement within the top and bottom y-faces is given by

$$D^{y+}(x,z) = \bar{D}_0^{y+} + \frac{\Delta_x D_0^{y+}}{\Delta x}x + \frac{\Delta_z D_0^{y+}}{\Delta z}z; \qquad D^{y-}(x,z) = \bar{D}_0^{y-} + \frac{\Delta_x D_0^{y-}}{\Delta x}x + \frac{\Delta_z D_0^{y-}}{\Delta z}z \tag{3.5}$$

Similarly, the *z*-component of the electric displacement within the top and bottom *z*-faces is given by

$$D^{z+}(x,y) = \bar{D}_0^{z+} + \frac{\Delta_x D_0^{z+}}{\Delta x}x + \frac{\Delta_y D_0^{z+}}{\Delta y}y; \qquad D^{z-}(x,y) = \bar{D}_0^{z-} + \frac{\Delta_x D_0^{z-}}{\Delta x}x + \frac{\Delta_y D_0^{z-}}{\Delta y}y \tag{3.6}$$

The reconstruction that we seek has to take this second order variation within the faces and obtain therefrom a second order accurate reconstructed vector field for the electric displacement within the volume shown in Fig. 1.

The vector field for the electric displacement that we wish to find within the zone shown in Fig. 1 is such that it satisfies eqn. (3.3) everywhere within the zone. It also exactly matches up with eqn. (3.4) at the top and bottom *x*-faces, eqn. (3.5) at the top and bottom *y*-faces and eqn. (3.6) at the top and bottom *z*-faces. By putting eqn. (3.2) into the right hand side of eqn. (3.3) we see that it provides four constraints. However, one of the four constraints is redundant because of eqn. (3.1). As a result, eqn. (3.3) effectively provides three independent constraints. Matching the variation at the top and bottom *x*-boundaries via eqn. (3.4) provides six further conditions. Likewise, matching the variation at the top and bottom *y*-boundaries via eqn. (3.5) provides six additional conditions. Similarly, matching the variation at the top and bottom *z*-boundaries via eqn. (3.6) gives yet another six conditions. We see, therefore, that the vector field for the electric displacement is specified by twenty-one independent coefficients. The lowest-order polynomial representation for the three components of the electric displacement vector field that enables us to meet all these requirements is given by

$$D^x(x,y,z) = a_0 + a_x\left(\frac{x}{\Delta x}\right) + a_y\left(\frac{y}{\Delta y}\right) + a_z\left(\frac{z}{\Delta z}\right)$$
$$+ a_{xx}\left(\left(\frac{x}{\Delta x}\right)^2 - \frac{1}{12}\right) + a_{xy}\left(\frac{x}{\Delta x}\right)\left(\frac{y}{\Delta y}\right) + a_{xz}\left(\frac{x}{\Delta x}\right)\left(\frac{z}{\Delta z}\right) \tag{3.7}$$

$$D^y(x,y,z) = b_0 + b_x\left(\frac{x}{\Delta x}\right) + b_y\left(\frac{y}{\Delta y}\right) + b_z\left(\frac{z}{\Delta z}\right)$$
$$+ b_{xy}\left(\frac{x}{\Delta x}\right)\left(\frac{y}{\Delta y}\right) + b_{yy}\left(\left(\frac{y}{\Delta y}\right)^2 - \frac{1}{12}\right) + b_{yz}\left(\frac{y}{\Delta y}\right)\left(\frac{z}{\Delta z}\right) \tag{3.8}$$

$$D^z(x,y,z) = c_0 + c_x\left(\frac{x}{\Delta x}\right) + c_y\left(\frac{y}{\Delta y}\right) + c_z\left(\frac{z}{\Delta z}\right)$$
$$+ c_{xz}\left(\frac{x}{\Delta x}\right)\left(\frac{z}{\Delta z}\right) + c_{yz}\left(\frac{y}{\Delta y}\right)\left(\frac{z}{\Delta z}\right) + c_{zz}\left(\left(\frac{z}{\Delta z}\right)^2 - \frac{1}{12}\right) \tag{3.9}$$

The terms in the above three polynomials are selected from symmetry and constraint-preserving considerations. The twenty-one independent coefficients in eqns. (3.7), (3.8) and (3.9) can be precisely specified by using the known coefficients in eqns. (3.2), (3.4), (3.5) and (3.6). The exact procedure for doing this is catalogued in Appendix C.

This completes our description of the constraint-preserving reconstruction. The constraint-preserving reconstruction is the first step that one does in a timestep loop. It takes the facially-collocated normal components of the electric displacement vector and the magnetic induction vector and give us two constraint-satisfying vector fields for the electric displacement and magnetic induction that are valid at any location in the computational domain. Moreover, these vector fields are constructed with due attention paid to non-oscillatory reconstruction as given by modern TVD or WENO methods.

Realize that a constraint-preserving reconstruction strategy can always revert back to a divergence-free reconstruction strategy when the divergence of the vector field is exactly zero. Therefore, the same strategy works without any further changes for the vector field for the magnetic induction. When magnetic charges are absent, the magnetic induction vector field will be globally divergence-free at all locations on the mesh. In the code, the two sets of vector fields are reconstructed by using the same set of subroutines. This constraint-preserving reconstruction strategy can also be extended to higher orders as we will show in a sequel paper.

Also notice that the first four terms in eqns. (3.7), (3.8) and (3.9) are needed for second-order accuracy. The other three terms in the same equations are needed for consistency. The reconstructed vector fields for the electric displacement and magnetic induction would not globally satisfy their constraints without the use of all the terms in those three equations. The first four terms in eqns. (3.7), (3.8) and (3.9) are, therefore, evolutionary and participate in the ADER time evolution step which we describe next.

4. Second-order-accurate ADER-DG scheme with sub-cell resolution of material properties and implicit treatment of stiff source terms

The previous Section has shown us how we can obtain two constraint-satisfying vector fields for the electric displacement and magnetic induction that are valid at any location in the computational domain. This means that we have

higher-order spatial derivatives within each zone for each of these two vector fields. We would like to know how these vector fields evolve for a short interval of time (in-the-small evolution) within each zone in a fashion that is consistent with the conservation law in eqn. (2.11). In this section, we present an ADER scheme that does precisely that.

We divide this section into three parts. We realize that ADER schemes have not been used much at all in CED. Therefore, Sub-section 4.1 provides background information and also explains at an intuitive level why the variant of ADER scheme presented here is so valuable for CED. Sub-section 4.2 presents the equations and the solution methodology. Sub-section 4.3 shows how the matrix inversion in the Newton step is considerably simplified in the ADER scheme that we present here. Sub-section 4.4 presents an extremely efficient treatment of stiff source terms in the limit where the permittivity and permeability matrices are diagonal.

4.1. Background on ADER schemes and their utility in CED

ADER schemes possess some very desirable properties. While the older ADER schemes by Toro, Millington and Nejad [53], Titarev and Toro [51,52] and Toro and Titarev [54] are not very well-suited to our specific needs in this paper, there is another variant of ADER schemes that have some very desirable properties. We refer to ADER schemes in predictor–corrector format (Dumbser et al. [27,28], Balsara et al. [6,9]). In this paper we have formulated ADER schemes to accommodate the treatment of stiff source terms in the predictor step. What makes this ADER formulation novel is the use of a minimal number of source term evaluations. The method can accommodate sub-cell variations in the source terms, as well as sub-cell variation in the coefficients of flux terms, which is exactly the feature we seek in this paper. It also minimizes the number of implicit source term evaluations. Having an absolute minimum number of source term evaluations is a very desirable attribute when the source terms have to be solved implicitly. The source-term treatment in our present ADER schemes is also provably A-stable. For that reason, we use ADER schemes in predictor–corrector format with implicit treatment of stiff source terms. The use of these novel ADER schemes that are specially adapted to the needs of computational electrodynamics in this paper is indeed the third major advance reported in this paper.

At a very intuitive level, we can think of the ADER predictor step as a kind of Lax–Wendroff (or Cauchy–Kovalevskaya) procedure that is applied to the governing PDE. In other words, given the spatial derivatives within a zone up to some order of accuracy, we wish to obtain time derivatives up to that same order of accuracy within that same zone. The time derivatives are obtained in such a way that they are consistent with the governing PDE. The ADER scheme that we describe here is also unlike a Lax–Wendroff procedure in the sense that the method is applied iteratively, with each iteration being very simple and computationally inexpensive. The iterations are known to converge fast. The present strategy also differs from the Lax–Wendroff procedure because it permits a pointwise implicit treatment of the stiff source terms. The implicit terms are solved with a Newton method, which also converges very fast. Let us examine how these issues, as well as allied issues, play out in CED.

There are two very important physics issues that are most challenging in CED. The first has to do with the fact that permittivity and permeability can undergo up to an order of magnitude change at the interface between dielectrics (Farjadpour et al. [31], Oskooi et al. [39], Taflove, Oskooi, and Johnson [49]). The second has to do with the fact that the conductivity can undergo very substantial variation. This may happen when analyzing skin-depth effects in a metal, but it occurs much more often when dealing with perfectly matched layers (PML) at the boundary of a computational domain (Berenger [20,21], Katz, Thiel and Taflove [36], Taflove and Hagness [48]). Let us, therefore, examine the consequences of such variation by focusing on the flux terms and source terms in eqn. (2.12). A through discussion of the issues will guide us to the optimal predictor step that enables us to make an evolution in-the-small for the equations of CED. We will then show that the particular variant of ADER scheme that we present here is the optimal response to those two vexatious physics issues. The ADER scheme that we present is optimal for CED in the following senses: 1) It includes the effects of sub-cell variation in the dielectric properties. 2) It permits the inclusion of very large conductivities without having any impact on the CFL number. 3) The implicit treatment of the source terms only requires the inversion of small 6×6 matrices; the older ADER schemes would have required the inversion of larger matrices. 4) When the permittivity and permeability tensors are diagonal, the 6×6 matrices mentioned above become diagonal, which further simplifies the matrix inversion. We should also mention that the ADER scheme presented here is very novel and we have not seen ADER schemes formulated in this way in the literature.

Let us first discuss the fact that the permittivity and permeability undergo dramatic sub-cell variations at dielectric interfaces. As a result, we can always take the matrices $\tilde{\varepsilon} \equiv \varepsilon^{-1}$ and $\tilde{\mu} \equiv \mu^{-1}$ and carry out a suitably high-order reconstruction of each of their components. But we need a scheme that directly incorporates the high-order reconstruction of the material tensors in the flux evaluation. From eqn. (2.12) we see that the material matrices play an important role in the fluxes. But, to capture the spatial variation in the material properties, we should have an ADER scheme that not just responds to the fluxes but is also responsive to the gradients of the fluxes. That way, at each nodal point where the fluxes are evaluated, we will also have to evaluate the gradients of the fluxes, which incorporate the variation of the matrices in question. We will, indeed, design such an ADER scheme. We now also realize an ancillary benefit that comes from using the normal components of the electric displacement and the magnetic induction as the primal variables – such a choice allows us to directly incorporate the variation of the material properties into the flux terms.

Second, we discuss the fact that at PML boundaries, or in some instances at metallic interfaces, we will have rapid sub-cell variations in the conductivity. In such cases, the electric and magnetic conductivities can become very large and also

have substantial variation within a zone. As a result, the ADER scheme should treat the source terms implicitly. But it should also incorporate the gradients of the source terms into the predictor step. We will, indeed, design such an ADER scheme. The ADER scheme that we present has a very desirable property that it couples only the source terms at a given spatial node. This reduces the size of the matrices that have to be inverted in the Newton step. Furthermore, as we will show, the resulting matrices can be manipulated into a form that only entails the inversion of block upper-triangular matrices. This simplifies the Newton step very considerably, especially at higher orders.

4.2. Description of our ADER scheme at second order

To facilitate our narrative, let us make a linear mapping of the space–time extent of each zone in its local coordinates given by $(x, y, z, t) \in [-\Delta x/2, \Delta x/2] \times [-\Delta y/2, \Delta y/2] \times [-\Delta z/2, \Delta z/2] \times [0, \Delta t]$ to the reference element given by $(\xi, \eta, \zeta, \tau) \in [-1/2, 1/2] \times [-1/2, 1/2] \times [-1/2, 1/2] \times [0, 1]$. With this linear mapping, the governing PDE becomes

$$\frac{\partial \mathbf{u}(\xi, \eta, \zeta, \tau)}{\partial \tau} + \frac{\partial \mathbf{f}(\xi, \eta, \zeta, \tau)}{\partial \xi} + \frac{\partial \mathbf{g}(\xi, \eta, \zeta, \tau)}{\partial \eta} + \frac{\partial \mathbf{h}(\xi, \eta, \zeta, \tau)}{\partial \zeta} = \mathbf{s}(\xi, \eta, \zeta, \tau) \tag{4.1}$$

where we have the slight redefinitions (and rescalings) given by $\mathbf{u}(\xi, \eta, \zeta, \tau) = \mathbf{U}(x, y, z, t)$, $\mathbf{f}(\xi, \eta, \zeta, \tau) = \Delta t \mathbf{F}(x, y, z, t)/\Delta x$, $\mathbf{g}(\xi, \eta, \zeta, \tau) = \Delta t \mathbf{G}(x, y, z, t)/\Delta y$, $\mathbf{h}(\xi, \eta, \zeta, \tau) = \Delta t \mathbf{K}(x, y, z, t)/\Delta z$ and $\mathbf{s}(\xi, \eta, \zeta, \tau) = \Delta t \mathbf{S}(x, y, z, t)$. Please note that we are making a small notational realignment in the nomenclature for the z-flux.

The electric displacement and the magnetic induction are the primal variables of our scheme. Now realize that the reconstruction from Section 3 has provided us with one three-component vector field for the electric displacement and another three-component vector field for the magnetic induction. This is shown in eqns. (3.7), (3.8) and (3.9). As discussed before, only the first four terms in each of the above-mentioned equations are time-evolutionary at second order of accuracy. As a result, consider a six-component vector $\bar{\mathbf{w}}$ of initial conditions that is defined at a node that resides at the zone center. The vector is filled with the constant part of eqns. (3.7), (3.8) and (3.9). The first three components of $\bar{\mathbf{w}}$ contain the constant parts of the electric displacement at the center of the zone; the next three components of $\bar{\mathbf{w}}$ contain the constant parts of the magnetic induction at the center of the zone. Furthermore, consider the six-component vector $(\partial_\xi \mathbf{w})$. This vector is filled with the x-variation from eqns. (3.7), (3.8) and (3.9) that has been suitably mapped to the reference element. The first three components of $(\partial_\xi \mathbf{w})$ contain the ξ-derivatives of the electric displacement at the center of the zone; the next three components of $(\partial_\xi \mathbf{w})$ contain the ξ-derivatives of the magnetic induction at the center of the zone. With this detailed description, the reader can understand how to initialize $(\partial_\eta \mathbf{w})$ and $(\partial_\zeta \mathbf{w})$ with suitable η-derivatives and ζ-derivatives of the solution vector. We can now write our initial conditions within each zone of the mesh as

$$\mathbf{w}(\xi, \eta, \zeta) = \bar{\mathbf{w}} + (\partial_\xi \mathbf{w})\xi + (\partial_\eta \mathbf{w})\eta + (\partial_\zeta \mathbf{w})\zeta \tag{4.2}$$

This explains to us in rather explicit terms how the vector of initial conditions is initialized at $\tau = 0$ for each zone of the mesh. We wish to evolve this initial condition in time in order to obtain a predictor step.

In the predictor step, we want to locate ourselves within each zone and use the initial spatial variation in the solution at $\tau = 0$ to obtain the time-evolution of the solution in-the-small within that same zone. In other words, during the ADER predictor step, each zone evolves for a short period of time by using its own internal values without paying attention to neighboring zones. We want to obtain the solution $\mathbf{u}(\xi, \eta, \zeta, \tau)$ implicitly in time so that it is defined at temporal nodal points given by $\tau_1 = 1/2$ and $\tau_2 = 1$. Those two nodal points are also centered in space at the zone center and have the same spatial modes at each time point as eqn. (4.2). Written explicitly, our two nodal points in space–time within the reference element are given by $(\xi, \eta, \zeta, \tau) = (0, 0, 0, 1/2)$ and $(\xi, \eta, \zeta, \tau) = (0, 0, 0, 1)$. Consequently, we can write the solution vector in space–time as

$$\mathbf{u}(\xi, \eta, \zeta, \tau) = \left(\mathbf{u}_1 + (\partial_\xi \mathbf{u}_1)\xi + (\partial_\eta \mathbf{u}_1)\eta + (\partial_\zeta \mathbf{u}_1)\zeta \right)(-2)(\tau - 1)$$
$$+ \left(\mathbf{u}_2 + (\partial_\xi \mathbf{u}_2)\xi + (\partial_\eta \mathbf{u}_2)\eta + (\partial_\zeta \mathbf{u}_2)\zeta \right)(2)(\tau - 1/2) \tag{4.3}$$

Let us interpret eqn. (4.3) in words because ADER schemes might not be familiar to the CED community. We see that $\mathbf{u}_1$, $(\partial_\xi \mathbf{u}_1)$, $(\partial_\eta \mathbf{u}_1)$ and $(\partial_\zeta \mathbf{u}_1)$ are the solution vector, its ξ-derivative, its η-derivative and its ζ-derivative respectively at the space–time nodal point given by $(\xi, \eta, \zeta, \tau) = (0, 0, 0, 1/2)$. We also see that $\mathbf{u}_2$, $(\partial_\xi \mathbf{u}_2)$, $(\partial_\eta \mathbf{u}_2)$ and $(\partial_\zeta \mathbf{u}_2)$ are the solution vector, its ξ-derivative, its η-derivative and its ζ-derivative respectively at the space–time nodal point given by $(\xi, \eta, \zeta, \tau) = (0, 0, 0, 1)$. The eight vectors (with each vector having six components) described in the previous two sentences are the modes of the scheme. In the parlance of Galerkin formulations, the set of eight trial functions, $\phi_i(\xi, \eta, \zeta, \tau)$ with $i = 1, .., 8$, is given by

$$\begin{cases} \phi_1(\xi, \eta, \zeta, \tau) = (-2)(\tau - 1), \ \phi_2(\xi, \eta, \zeta, \tau) = (-2)(\tau - 1)\xi, \ \phi_3(\xi, \eta, \zeta, \tau) = (-2)(\tau - 1)\eta, \\ \phi_4(\xi, \eta, \zeta, \tau) = (-2)(\tau - 1)\zeta, \ \phi_5(\xi, \eta, \zeta, \tau) = (2)(\tau - 1/2), \ \phi_6(\xi, \eta, \zeta, \tau) = (2)(\tau - 1/2)\xi, \\ \phi_7(\xi, \eta, \zeta, \tau) = (2)(\tau - 1/2)\eta, \ \phi_8(\xi, \eta, \zeta, \tau) = (2)(\tau - 1/2)\zeta \end{cases} \tag{4.4}$$

We will use test functions that are also defined from the above set of trial functions.

We see that eqn. (4.3) is very suitable for an iterative Galerkin method because the modes are indeed the desired solution vector and its derivatives at each of the two nodal points in space–time. As a result, when the modes in eqn. (4.3)

are improved during the course of each iteration, we can also use the modes to obtain the improved fluxes and their derivatives at each of those nodal points in space–time. To take an example, given an improved set of four vectors, $\mathbf{u}_1$, $(\partial_\xi \mathbf{u}_1)$, $(\partial_\eta \mathbf{u}_1)$, and $(\partial_\zeta \mathbf{u}_1)$ at space–time node "1", we can use eqn. (2.12) and our rescaling of the fluxes to evaluate an improved set of ξ-fluxes and their derivatives given by $\mathbf{f}_1$, $(\partial_\xi \mathbf{f}_1)$, $(\partial_\eta \mathbf{f}_1)$ and $(\partial_\zeta \mathbf{f}_1)$. We can do similarly at space–time node "2". This enables us to write an expression for the ξ-flux that is analogous to eqn. (4.3) as follows

$$\mathbf{f}(\xi, \eta, \zeta, \tau) = \big(\mathbf{f}_1 + (\partial_\xi \mathbf{f}_1)\xi + (\partial_\eta \mathbf{f}_1)\eta + (\partial_\zeta \mathbf{f}_1)\zeta\big)(-2)(\tau - 1)$$
$$+ \big(\mathbf{f}_2 + (\partial_\xi \mathbf{f}_2)\xi + (\partial_\eta \mathbf{f}_2)\eta + (\partial_\zeta \mathbf{f}_2)\zeta\big)(2)(\tau - 1/2) \tag{4.5}$$

We can do similarly for the η- and ζ-fluxes in the next two equations

$$\mathbf{g}(\xi, \eta, \zeta, \tau) = \big(\mathbf{g}_1 + (\partial_\xi \mathbf{g}_1)\xi + (\partial_\eta \mathbf{g}_1)\eta + (\partial_\zeta \mathbf{g}_1)\zeta\big)(-2)(\tau - 1)$$
$$+ \big(\mathbf{g}_2 + (\partial_\xi \mathbf{g}_2)\xi + (\partial_\eta \mathbf{g}_2)\eta + (\partial_\zeta \mathbf{g}_2)\zeta\big)(2)(\tau - 1/2) \tag{4.6}$$

and

$$\mathbf{h}(\xi, \eta, \zeta, \tau) = \big(\mathbf{h}_1 + (\partial_\xi \mathbf{h}_1)\xi + (\partial_\eta \mathbf{h}_1)\eta + (\partial_\zeta \mathbf{h}_1)\zeta\big)(-2)(\tau - 1)$$
$$+ \big(\mathbf{h}_2 + (\partial_\xi \mathbf{h}_2)\xi + (\partial_\eta \mathbf{h}_2)\eta + (\partial_\zeta \mathbf{h}_2)\zeta\big)(2)(\tau - 1/2) \tag{4.7}$$

Formally, we can write the source terms in the same fashion as

$$\mathbf{s}(\xi, \eta, \zeta, \tau) = \big(\mathbf{s}_1 + (\partial_\xi \mathbf{s}_1)\xi + (\partial_\eta \mathbf{s}_1)\eta + (\partial_\zeta \mathbf{s}_1)\zeta\big)(-2)(\tau - 1)$$
$$+ \big(\mathbf{s}_2 + (\partial_\xi \mathbf{s}_2)\xi + (\partial_\eta \mathbf{s}_2)\eta + (\partial_\zeta \mathbf{s}_2)\zeta\big)(2)(\tau - 1/2) \tag{4.8}$$

Because we wish to treat the source terms implicitly, we will of course evaluate the vectors $\mathbf{s}_1$ and $\mathbf{s}_2$ somewhat differently. This will become clearer in the next few paragraphs where we involve the governing equation, eqn. (4.1), and see what it gives us.

The governing equation, eqn. (4.1), regulates the time-evolution of the PDE system. It, therefore, controls the dynamics. If we want to iteratively improve the solution vector itself, we should involve the governing equation in the iteration step. In other words, an improved iterate for eqn. (4.3) can only be obtained if we involve eqn. (4.1). This is most easily done by using our test functions to make a Galerkin projection in space–time of the governing equation. In other words, let $\phi_i(\xi, \eta, \zeta, \tau)$ with $i = 1, .., 8$ be one of the eight test functions from eqn. (4.4). For $i = 1, .., 8$ we then demand that

$$\int_0^1 \left\{ \int_{-1/2}^{1/2} \left\{ \int_{-1/2}^{1/2} \left\{ \int_{-1/2}^{1/2} \left\{ \phi_i(\xi, \eta, \zeta, \tau) \left[\begin{array}{l} \dfrac{\partial \mathbf{u}(\xi, \eta, \zeta, \tau)}{\partial \tau} + \dfrac{\partial \mathbf{f}(\xi, \eta, \zeta, \tau)}{\partial \xi} \\ + \dfrac{\partial \mathbf{g}(\xi, \eta, \zeta, \tau)}{\partial \eta} + \dfrac{\partial \mathbf{h}(\xi, \eta, \zeta, \tau)}{\partial \zeta} - \mathbf{s}(\xi, \eta, \zeta, \tau) \end{array} \right] \right\} d\xi \right\} d\eta \right\} d\zeta \right\} d\tau = 0 \tag{4.9}$$

Please note that the square bracket in the previous equation is not a matrix. In the above equation, we are simply projecting the governing equation, i.e. eqn. (4.1), into the space of test functions and demanding that the projection is zero. Operationally, to carry out the Galerkin projection, we simply insert eqns. (4.3), (4.5), (4.6), (4.7) and (4.8) into the square bracket in eqn. (4.9). We then use a computer algebra system to carry out the four-dimensional space–time integrals. The computer algebra system is further asked to simplify the resulting eight conditions that we get from eqn. (4.9). After a little bit of dexterous manipulation with the computer algebra system, we get eight very elegant, and very simple, evolutionary equations which we will describe in the next paragraph.

The evolutionary equations that we obtain at node "1" are given by

$$\mathbf{u}_1 = \bar{\mathbf{w}} + \frac{4}{6}\mathbf{s}_1 - \frac{1}{6}\mathbf{s}_2 - \frac{4}{6}\big((\partial_\xi \mathbf{f}_1) + (\partial_\eta \mathbf{g}_1) + (\partial_\zeta \mathbf{h}_1)\big) + \frac{1}{6}\big((\partial_\xi \mathbf{f}_2) + (\partial_\eta \mathbf{g}_2) + (\partial_\zeta \mathbf{h}_2)\big) \tag{4.10}$$

$$(\partial_\xi \mathbf{u}_1) = (\partial_\xi \mathbf{w}) + \frac{4}{6}(\partial_\xi \mathbf{s}_1) - \frac{1}{6}(\partial_\xi \mathbf{s}_2) \tag{4.11}$$

$$(\partial_\eta \mathbf{u}_1) = (\partial_\eta \mathbf{w}) + \frac{4}{6}(\partial_\eta \mathbf{s}_1) - \frac{1}{6}(\partial_\eta \mathbf{s}_2) \tag{4.12}$$

$$(\partial_\zeta \mathbf{u}_1) = (\partial_\zeta \mathbf{w}) + \frac{4}{6}(\partial_\zeta \mathbf{s}_1) - \frac{1}{6}(\partial_\zeta \mathbf{s}_2) \tag{4.13}$$

The evolutionary equations that we obtain at node "2" are given by

$$\mathbf{u}_2 = \bar{\mathbf{w}} + \mathbf{s}_1 - \big((\partial_\xi \mathbf{f}_1) + (\partial_\eta \mathbf{g}_1) + (\partial_\zeta \mathbf{h}_1)\big) \tag{4.14}$$

$$(\partial_\xi \mathbf{u}_2) = (\partial_\xi \mathbf{w}) + (\partial_\xi \mathbf{s}_1) \tag{4.15}$$

$$(\partial_\eta \mathbf{u}_2) = (\partial_\eta \mathbf{w}) + (\partial_\eta \mathbf{s}_1) \tag{4.16}$$

$$(\partial_\zeta \mathbf{u}_2) = (\partial_\zeta \mathbf{w}) + (\partial_\zeta \mathbf{s}_1) \tag{4.17}$$

If the source terms are not stiff in a given zone, these equations can be used as-is. Notice that the use of the gradients of the fluxes in eqn. (4.10) and (4.14) ensures that the gradients of the material properties within a zone are accounted for in the update. Also notice that eqns. (4.11) to (4.13) and also eqns. (4.15) to (4.17) do not depend on the gradients of the fluxes but they depend only on the gradients of the source terms. We see, therefore, that gradients in the source terms can influence the gradients in the solution. The gradients in the solution can, in turn, influence the gradients of the fluxes and, consequently, the evolution of eqns. (4.10) and (4.14).

When the source terms are stiff, a minimum requirement is that eqns. (4.10) and (4.14) have to be solved implicitly. In that case, it helps to realize that the source term $\mathbf{s}_1$ depends on the state $\mathbf{u}_1$. Likewise, the source term $\mathbf{s}_2$ depends on the state $\mathbf{u}_2$. Thus, in the course of constructing a Newton sub-iteration, we will have to construct the Jacobian of these source terms with respect to the states. Let us define the following residual terms

$$R_1 = -\mathbf{u}_1 + \bar{\mathbf{w}} + \frac{4}{6}\mathbf{s}_1 - \frac{1}{6}\mathbf{s}_2 - \frac{4}{6}\big((\partial_\xi \mathbf{f}_1) + (\partial_\eta \mathbf{g}_1) + (\partial_\zeta \mathbf{h}_1)\big) + \frac{1}{6}\big((\partial_\xi \mathbf{f}_2) + (\partial_\eta \mathbf{g}_2) + (\partial_\zeta \mathbf{h}_2)\big) \tag{4.18}$$

and

$$R_2 = -\mathbf{u}_2 + \bar{\mathbf{w}} + \mathbf{s}_1 - \big((\partial_\xi \mathbf{f}_1) + (\partial_\eta \mathbf{g}_1) + (\partial_\zeta \mathbf{h}_1)\big) \tag{4.19}$$

The sub-iteration within each iterative step should drive $R_1 \to 0$ and $R_2 \to 0$. This calls for a root solver and we choose a Newton method. Each sub-iteration produces increments to the states $\mathbf{u}_1$ and $\mathbf{u}_2$, which we denote by $\delta\mathbf{u}_1$ and $\delta\mathbf{u}_2$. These increments are added to the original states and drive the solution closer to convergence. This root-solving process can be implemented in code by introducing one or more Newton sub-steps within each outer ADER iteration step. (We have found one Newton sub-step to be sufficient.) The presence of $\mathbf{s}_2$ in eqn. (4.18), along with the presence of $\mathbf{s}_1$ in eqn. (4.19) would suggest that we will have to solve the two equations simultaneously in a Newton step. Let $(\partial_\mathbf{u}\mathbf{s}_1)$ denote the Jacobian of the source $\mathbf{s}_1$ with respect to the state $\mathbf{u}_1$. Let $(\partial_\mathbf{u}\mathbf{s}_2)$ denote the Jacobian of the source $\mathbf{s}_2$ with respect to the state $\mathbf{u}_2$. The Newton step for eqns. (4.18) and (4.19) gives us the 12×12 matrix equation for the increments $\delta\mathbf{u}_1$ and $\delta\mathbf{u}_2$

$$\begin{pmatrix} \mathbf{I} - \frac{4}{6}(\partial_\mathbf{u}\mathbf{s}_1) & \frac{1}{6}(\partial_\mathbf{u}\mathbf{s}_2) \\ -(\partial_\mathbf{u}\mathbf{s}_1) & \mathbf{I} \end{pmatrix} \begin{pmatrix} \delta\mathbf{u}_1 \\ \delta\mathbf{u}_2 \end{pmatrix} = \begin{pmatrix} R_1 \\ R_2 \end{pmatrix} \tag{4.20}$$

Here $\mathbf{I}$ is a 6×6 identity matrix. After each sub-iteration from eqn. (4.20) we set $\mathbf{u}_1 \to \mathbf{u}_1 + \delta\mathbf{u}_1$ and $\mathbf{u}_2 \to \mathbf{u}_2 + \delta\mathbf{u}_2$. A naïve assessment of eqn. (4.20) suggests that we would have to invert a 12×12 matrix in the Newton sub-iteration step. In the next sub-section, we bring out one of the hidden benefits of our ADER approach by showing that the Newton sub-iteration only requires the solution of one 6×6 matrix equation, which is a substantially less expensive undertaking. In the next Sub-section we show that this simplification results from shrewdly exploiting the matrix structure of eqn. (4.20).

This completes our description of the ADER equations as well as our set-up for their implicit solution. The ADER scheme is the second logical step that gets invoked in a timestep loop for CED. We start with spatial derivatives for the primal variables within each zone and we wind up with an in-the-small evolution in time for such variables within each zone, thanks to the ADER scheme. Now those zones need to interact with one another. This sets the stage for the next Sub-section which deals with the multidimensional Riemann solver.

Notice too that a converged solution also gives us the space–time representation of the source terms within each zone from eqn. (4.8). These source terms have been updated via an implicit update in the case where the source terms are stiff. Each zone boundary, where the sources due to the currents are needed, has two zones abutting it. The properly implicited source term at each boundary can be obtained by evaluating the space–time averaged version of the source terms from both of the zones that abut the zone-boundary of interest. These space–time averages from either side of a zone boundary are then arithmetically averaged and assigned to the zone-boundary that we are interested in. This completes our description of the ADER scheme's role in enabling a proper treatment of the stiff, face-averaged source terms.

It is also possible to use a strong stability preserving Runge–Kutta (SSP-RK) method for CED (Balsara et al. [16]). The stiffness in the source terms can be accommodated at high order of accuracy via such methods. However, the sub-cell variation in the flux terms cannot be accommodated by such methods. This is why the ADER predictor step followed by a corrector step and a one-step update might have an advantage over SSP-RK methods in CED. For the sake of completeness, for time-explicit SSP-RK methods, see Shu and Osher [44,45], Shu [46] and Spiteri and Ruuth [42,43]; for implicit–explicit SSP-RK methods, see Pareschi and Russo [40], Hunsdorfer and Ruuth [33] and Kupka et al. [37].

4.3. Computationally efficient treatment of the Newton sub-iteration

First realize that the matrix in eqn. (4.20) is a 12×12 matrix with a special inner structure. It is very easy to transform the diagonal terms to identity by taking $-4/6$ times the second row and adding it to the first row. Eqn. (4.20) then becomes

$$\begin{pmatrix} \mathbf{I} & \frac{1}{6}(\partial_\mathbf{u}\mathbf{s}_2) - \frac{4}{6}\mathbf{I} \\ -(\partial_\mathbf{u}\mathbf{s}_1) & \mathbf{I} \end{pmatrix} \begin{pmatrix} \delta\mathbf{u}_1 \\ \delta\mathbf{u}_2 \end{pmatrix} = \begin{pmatrix} R_1 - \frac{4}{6}R_2 \\ R_2 \end{pmatrix} \tag{4.21}$$

Next, we left-multiply the first row by $(\partial_\mathbf{u}\mathbf{s}_1)$ and add it to the second row to get

$$\begin{pmatrix} \mathbf{I} & \frac{1}{6}(\partial_\mathbf{u}\mathbf{s}_2) - \frac{4}{6}\mathbf{I} \\ 0 & \mathbf{I} + (\partial_\mathbf{u}\mathbf{s}_1)(\frac{1}{6}(\partial_\mathbf{u}\mathbf{s}_2) - \frac{4}{6}\mathbf{I}) \end{pmatrix} \begin{pmatrix} \delta\mathbf{u}_1 \\ \delta\mathbf{u}_2 \end{pmatrix} = \begin{pmatrix} R_1 - \frac{4}{6}R_2 \\ R_2 + (\partial_\mathbf{u}\mathbf{s}_1)(R_1 - \frac{4}{6}R_2) \end{pmatrix} \tag{4.22}$$

The upper triangular structure of the matrix in eqn. (4.22) is clearly displayed. The lower row in eqn. (4.22) can be solved for $\delta\mathbf{u}_2$ by solving a single 6×6 linear system. The resulting $\delta\mathbf{u}_2$ can be inserted into the first row of eqn. (4.22). This gives us a solution for $\delta\mathbf{u}_1$. This completes our description of a computationally efficient treatment of the stiff source terms in the ADER predictor step.

Notice the 6×6 identity matrices on the diagonal of eqn. (4.21). They suggest that if the problem is well-scaled then the diagonal elements of eqn. (4.21) can serve as a good pivot. We cannot prove that this is so, however, we have carried out extensive numerical experiments with eqns. (4.20), (4.21) and (4.22) where we solved several linear and non-linear systems by direct inversion of eqn. (4.20) as well as the method presented in eqn. (4.22) along with the narrative immediately after it. In all our tests, as long as the eigenvalues of $(\partial_{\mathbf{u}}\mathbf{s}_1)$ and $(\partial_{\mathbf{u}}\mathbf{s}_2)$ were negative, we found identical results and identical convergence rates. Direct inversion of eqn. (4.20), of course, costs much more than the method in eqn. (4.22). Also please note that requiring that the eigenvalues of $(\partial_{\mathbf{u}}\mathbf{s}_1)$ and $(\partial_{\mathbf{u}}\mathbf{s}_2)$ are negative is crucial for the physics of stably solving any PDE. From the structure of the source terms in eqn. (2.12), we see that this is guaranteed for CED.

When the source terms are extremely stiff, as in a conductor, it is also useful to have an implicit treatment of the derivative terms in eqns. (4.11), (4.12), (4.13), (4.15), (4.16) and (4.17). Eqn. (4.11) and (4.15) form a pair and can be solved simultaneously. In fact, they result in the same matrix system as the one solved in this section. As a result, the same upper triangular matrix from eqn. (4.22) can be reused for the implicit treatment of the gradient terms. We will show in a subsequent paper that this is a common theme in all the ADER schemes (even at higher orders) that are designed according to the principles adopted here. As a result, this family of ADER schemes is special because it has an in-built efficiency in the treatment of stiff source terms.

4.4. Extremely efficient treatment of the source terms for diagonal permittivity and permeability matrices

The solution of eqns. (4.10) and (4.14) can be significantly simplified when the permittivity and permeability tensors are diagonal. Since this is also the case that occurs most frequently in practice, we specialize an explicit solution strategy for that case. In that case, from eqn. (2.12), we have $J_x = \sigma\tilde{\varepsilon}_{xx}D_x$, $J_y = \sigma\tilde{\varepsilon}_{yy}D_y$ and $J_z = \sigma\tilde{\varepsilon}_{zz}D_z$, with analogous terms for the magnetic current density (if it is present). Let us define the following right hand side terms

$$\tilde{R}_1 = \bar{\mathbf{w}} - \frac{4}{6}\big((\partial_\xi\mathbf{f}_1) + (\partial_\eta\mathbf{g}_1) + (\partial_\zeta\mathbf{h}_1)\big) + \frac{1}{6}\big((\partial_\xi\mathbf{f}_2) + (\partial_\eta\mathbf{g}_2) + (\partial_\zeta\mathbf{h}_2)\big) \tag{4.23}$$

and

$$\tilde{R}_2 = \bar{\mathbf{w}} - \big((\partial_\xi\mathbf{f}_1) + (\partial_\eta\mathbf{g}_1) + (\partial_\zeta\mathbf{h}_1)\big) \tag{4.24}$$

We get the solution for $\mathbf{u}_1$ and $\mathbf{u}_2$ as

$$\mathbf{u}_1 = \mathbf{P}^{-1}\left(\tilde{R}_1 - \frac{1}{6}\mathbf{Q}\tilde{R}_2\right); \qquad \mathbf{u}_2 = \mathbf{Q}\mathbf{u}_1 + \tilde{R}_2$$

$$\text{where} \quad \mathbf{P} \equiv \mathbf{I} - \frac{4}{6}\mathbf{Q} + \frac{1}{6}\mathbf{Q}^2$$

$$\text{and} \quad \mathbf{Q} \equiv \text{diag}\big(-\Delta t\sigma\tilde{\varepsilon}_{xx}, -\Delta t\sigma\tilde{\varepsilon}_{yy}, -\Delta t\sigma\tilde{\varepsilon}_{zz}, -\Delta t\sigma^*\tilde{\mu}_{xx}, -\Delta t\sigma^*\tilde{\mu}_{yy}, -\Delta t\sigma^*\tilde{\mu}_{zz}\big) \tag{4.25}$$

Because the inverse of a diagonal matrix is very simple to evaluate, we see that the fully implicit treatment of stiff source terms in CED is easy to implement and computationally inexpensive when the permittivity and permeability tensors are diagonal.

When the source terms are extremely stiff, as in a conductor, it is also useful to have an implicit treatment of eqns. (4.11), (4.12), (4.13), (4.15), (4.16) and (4.17), which carry the derivative information. Notice that eqns. (4.11) and (4.15) couple exclusively to one another; similarly for eqns. (4.12) and (4.16); likewise for eqns. (4.13) and (4.17). Consequently, we only need to describe a solution strategy for eqns. (4.11) and (4.15). In the case where the permittivity and permeability tensors are diagonal, this is especially simple. For a conductor, using diagonal permittivity and permeability tensors is usually an excellent approximation. The solution for eqns. (4.11) and (4.15) then becomes

$$(\partial_\xi\mathbf{u}_1) = \mathbf{P}^{-1}\left(\mathbf{I} - \frac{1}{6}\mathbf{Q}\right)(\partial_\xi\mathbf{w}); \qquad (\partial_\xi\mathbf{u}_2) = \mathbf{Q}(\partial_\xi\mathbf{u}_1) + (\partial_\xi\mathbf{w}) \tag{4.26}$$

We see, therefore, that a fully implicit treatment of the gradients of stiff source terms in CED is also easy to implement and computationally inexpensive in the limit where the permittivity and permeability tensors are diagonal.

5. An efficient multidimensional Riemann solver for Maxwell's equations

The previous ADER step has given us an in-the-small space–time representation of the primal variables within each zone. However, we are dealing with a hyperbolic system where all the zones interact with one another to yield the edge-collocated magnetic and electric fields shown in Fig. 1. The multidimensional Riemann solver, described in this Section, mediates that interaction in a truly multidimensionally upwind fashion.
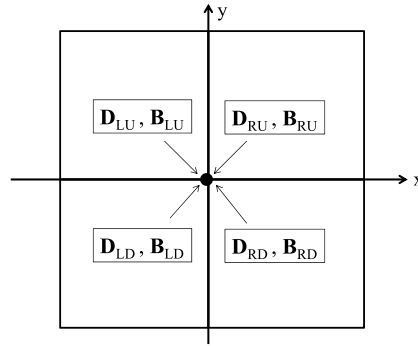
Fig. 2. The figure shows four zones in the xy-plane that come together at the z-edge of a three-dimensional mesh. Since the mesh is viewed from the top in plan view, the z-edge is shown by the black dot and the four abutting zones are shown as four squares. The four states have subscripts given by "RU" for right-upper; "LU" for left-upper; "LD" for left-down and "RD" for right-down. Fig. 2 shows the situation before the states start interacting via four one-dimensional and one multidimensional Riemann problems. The arrows indicate that higher-order reconstruction is used to obtain the four states at the z-edge.
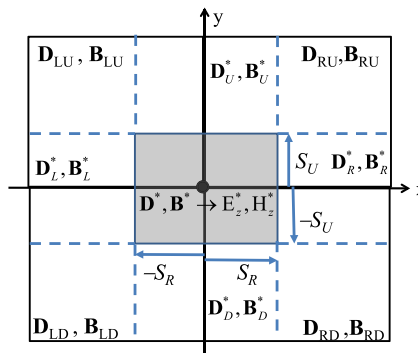

Fig. 3. The figure shows the same situation as Fig. 2. However, it shows the situation after the four incoming states start interacting with each other. Four one-dimensional Riemann problems, shown by dashed lines, develop between the four pairs of states. The shaded region depicts the strongly interacting state that arises when the four one-dimensional Riemann problems interact with one another. We want to find the z-component of the electric and magnetic fields in the strongly interacting state.

Multidimensional Riemann solvers that are easy to implement have reached a level of maturity (Balsara [7,8,11,14], Balsara, Dumbser and Abgrall [10], Balsara and Dumbser [13], Balsara et al. [15]). These Riemann solvers are also called **MuSIC** Riemann solvers because they are based on a **Mu**ltidimensional **S**elf-similar strongly-**I**nteracting state that is **C**onsistent with the PDE system. For Maxwell's equations, we design the simplest MuSIC Riemann solver without any sub-structure in the strongly interacting state. The reason for ignoring sub-structure is that all the waves arising from Maxwell's equations move very fast relative to the mesh and none of them can be stationary on the computational mesh. As a result, the sub-structure (that plays an important role in crisply capturing stationary discontinuities on the mesh) is not very important.

We restrict attention to Cartesian meshes in this paper; extension to unstructured meshes will be undertaken later. The two-dimensional Riemann solver lives at the edges of the mesh. It takes four states as its input, as shown in Fig. 2. These four states interact with each other resulting in four one-dimensional Riemann problems, as shown in Fig. 3. These four one-dimensional Riemann problems interact with one another, giving rise to the shaded strongly-interacting state in Fig. 3. For Maxwell's equations, this strongly-interacting state always overlies the edge being considered with the result that it is the correct physical state to assign to the edges of the mesh. It is, therefore, also the correct state that is to be used in the update of the two curl equations. We do not repeat the conceptual underpinnings for multidimensional Riemann solvers. We just operationally describe the process of obtaining the strongly-interacting state. We give sufficient information for handling the general case when the permittivity and permeability are full 3×3 tensors. In the limit when the permittivity and magnetic permeability are diagonal tensors, we also provide explicit formulae for the edge-centered electric and magnetic fields and provide a detailed discussion of their numerical dissipation.

We only need a two-dimensional Riemann solver to achieve proper upwinding at the edges of the mesh. We focus on the z-edge of the mesh. For the purposes of defining a multidimensional Riemann solver in the xy-plane, we only need to focus on the portion of the PDE system given by $\partial_t \mathbf{U} + \partial_x \mathbf{F} + \partial_y \mathbf{G} = 0$. The four states coming together at the vertex in question have subscripts RU (for right-upper), LU (for left-upper), LD (for left-down) and RD (for right-down) and are shown for the specific case of Maxwell's equations in Fig. 2. Fig. 2 depicts the incoming states at the z-edge of the mesh before the states have had a chance to interact. While we conceptualize four constant states interacting in the two-dimensional Riemann problem, in reality, the four states are obtained from a higher order reconstruction within the four zones shown in Fig. 2.

The arrows in Fig. 2 are meant to suggest that the higher order reconstruction is carried out in each zone and the four input states are obtained by evaluating the reconstructed variables at the edge being considered.

An analysis of the characteristic matrix associated with the x-flux shows that the extremal right-going speed is easy to find. For diagonal material tensors, please see eqn. (2.13) to realize that the extremal right-going speed is given by $S_R \equiv \max(\sqrt{\tilde{\mu}_{zz}\tilde{\varepsilon}_{yy}}, \sqrt{\tilde{\mu}_{yy}\tilde{\varepsilon}_{zz}})$ whereas the extremal left-going speed is given by $-S_R$. For material tensors with off-diagonal components, eqn. (2.15) enables us to identify the extremal right-going speed as $S_R \equiv \max(\sqrt{\tau^x - \chi^x\sqrt{\kappa^x}}/\sqrt{2}, \sqrt{\tau^x + \chi^x\sqrt{\kappa^x}}/\sqrt{2})$, with the extremal left-going speed given by $-S_R$. This enables us to identify the bounding speeds of any one-dimensional Riemann solver that operates in the x-direction. Please see Fig. 3 which shows the situation after the input states in Fig. 2 have been allowed to interact. Here we will use the simplest one-dimensional HLL (or LLF) Riemann solver with only one intermediate state. Consequently, between the right-upper and left-upper states we have a resolved HLL state that can be explicitly written as

$$
\mathbf{U}_U^* \equiv \begin{pmatrix} D_{x;U}^* \\ D_{y;U}^* \\ D_{z;U}^* \\ B_{x;U}^* \\ B_{y;U}^* \\ B_{z;U}^* \end{pmatrix}
$$

$$
= \begin{pmatrix} (D_{x;RU} + D_{x;LU})/2 \\ (D_{y;RU} + D_{y;LU})/2 - [\tilde{\mu}_{xz}(B_{x;RU} - B_{x;LU}) + \tilde{\mu}_{yz}(B_{y;RU} - B_{y;LU}) + \tilde{\mu}_{zz}(B_{z;RU} - B_{z;LU})]/(2S_R) \\ (D_{z;RU} + D_{z;LU})/2 + [\tilde{\mu}_{xy}(B_{x;RU} - B_{x;LU}) + \tilde{\mu}_{yy}(B_{y;RU} - B_{y;LU}) + \tilde{\mu}_{yz}(B_{z;RU} - B_{z;LU})]/(2S_R) \\ (B_{x;RU} + B_{x;LU})/2 \\ (B_{y;RU} + B_{y;LU})/2 + [\tilde{\varepsilon}_{xz}(D_{x;RU} - D_{x;LU}) + \tilde{\varepsilon}_{yz}(D_{y;RU} - D_{y;LU}) + \tilde{\varepsilon}_{zz}(D_{z;RU} - D_{z;LU})]/(2S_R) \\ (B_{z;RU} + B_{z;LU})/2 - [\tilde{\varepsilon}_{xy}(D_{x;RU} - D_{x;LU}) + \tilde{\varepsilon}_{yy}(D_{y;RU} - D_{y;LU}) + \tilde{\varepsilon}_{yz}(D_{z;RU} - D_{z;LU})]/(2S_R) \end{pmatrix} \tag{5.1}
$$

Between the right-down and left-down states we have a resolved HLL state that can be explicitly written by changing the subscript "U" to the subscript "D" in the above equation. Call that state $\mathbf{U}_D^*$. When the permittivity and permeability tensors are diagonal, a simpler version of eqn. (5.1) can be written.

An analysis of the characteristic matrix associated with the y-flux shows that the extremal upward-going speed is easy to find. For diagonal material tensors, please see eqn. (2.14) to realize that the extremal upward-going speed is given by $S_U \equiv \max(\sqrt{\tilde{\mu}_{xx}\tilde{\varepsilon}_{zz}}, \sqrt{\tilde{\mu}_{zz}\tilde{\varepsilon}_{xx}})$ whereas the extremal downward-going speed is given by $-S_U$. For material tensors with off-diagonal components, eqn. (2.16) enables us to identify the extremal upward-going speed as $S_U \equiv \max(\sqrt{\tau^y - \chi^y\sqrt{\kappa^y}}/\sqrt{2}, \sqrt{\tau^y + \chi^y\sqrt{\kappa^y}}/\sqrt{2})$, with the extremal downward-going speed given by $-S_U$. This enables us to identify the bounding speeds of any one-dimensional Riemann solver that operates in the y-direction. Consequently, between the right-upper and right-down states we have a resolved HLL state that can be explicitly written as

$$
\mathbf{U}_R^* \equiv \begin{pmatrix} D_{x;R}^* \\ D_{y;R}^* \\ D_{z;R}^* \\ B_{x;R}^* \\ B_{y;R}^* \\ B_{z;R}^* \end{pmatrix}
$$

$$
= \begin{pmatrix} (D_{x;RU} + D_{x;RD})/2 + [\tilde{\mu}_{xz}(B_{x;RU} - B_{x;RD}) + \tilde{\mu}_{yz}(B_{y;RU} - B_{y;RD}) + \tilde{\mu}_{zz}(B_{z;RU} - B_{z;RD})]/(2S_U) \\ (D_{y;RU} + D_{y;RD})/2 \\ (D_{z;RU} + D_{z;RD})/2 - [\tilde{\mu}_{xx}(B_{x;RU} - B_{x;RD}) + \tilde{\mu}_{xy}(B_{y;RU} - B_{y;RD}) + \tilde{\mu}_{xz}(B_{z;RU} - B_{z;RD})]/(2S_U) \\ (B_{x;RU} + B_{x;RD})/2 - [\tilde{\varepsilon}_{xz}(D_{x;RU} - D_{x;RD}) + \tilde{\varepsilon}_{yz}(D_{y;RU} - D_{y;RD}) + \tilde{\varepsilon}_{zz}(D_{z;RU} - D_{z;RD})]/(2S_U) \\ (B_{y;RU} + B_{y;RD})/2 \\ (B_{z;RU} + B_{z;RD})/2 + [\tilde{\varepsilon}_{xx}(D_{x;RU} - D_{x;RD}) + \tilde{\varepsilon}_{xy}(D_{y;RU} - D_{y;RD}) + \tilde{\varepsilon}_{xz}(D_{z;RU} - D_{z;RD})]/(2S_U) \end{pmatrix} \tag{5.2}
$$

Between the left-up and left-down states we have a resolved HLL state that can be explicitly written by changing the subscript "R" to the subscript "L" in the above equation. Call that state $\mathbf{U}_L^*$. When the permittivity and permeability tensors are diagonal, a simpler version of eqn. (5.2) can be written.

The strongly-interacting state, $\mathbf{U}^* \equiv \left(D_x^*, D_y^*, D_z^*, B_x^*, B_y^*, B_z^* \right)^T$, in Fig. 3 is shown by the grey shaded region. It is the state that overlies the z-edge of the mesh. It is, therefore, the state that will provide the resolved electric and magnetic fields at the z-edge that get used for the curl-type update shown in Fig. 1. The previous two paragraphs have shown us how to obtain the four state vectors ($\mathbf{U}_R^*$, $\mathbf{U}_U^*$, $\mathbf{U}_L^*$ and $\mathbf{U}_D^*$) that surround the strongly-interacting state in Fig. 3. For each of those states, we can use eqn. (2.12) to evaluate the corresponding fluxes. We use the state vector $\mathbf{U}_R^*$ to obtain the x-flux vector $\mathbf{F}_R^*$; likewise, we use the state vector $\mathbf{U}_L^*$ to obtain the x-flux vector $\mathbf{F}_L^*$. We also use the state vector $\mathbf{U}_U^*$ to obtain the

y-flux vector $\mathbf{G}^*_U$; similarly, we use the state vector $\mathbf{U}^*_D$ to obtain the y-flux vector $\mathbf{G}^*_D$. Using eqn. (12) in Balsara (2014) enables us to obtain the strongly-interacting state $\mathbf{U}^*$. In terms of the notation used here, that equation becomes

$$\mathbf{U}^* = -\frac{1}{4S_R}\big[\mathbf{F}^*_R - S_R\mathbf{U}^*_R\big] + \frac{1}{4S_R}\big[\mathbf{F}^*_L + S_R\mathbf{U}^*_L\big] - \frac{1}{4S_U}\big[\mathbf{G}^*_U - S_U\mathbf{U}^*_U\big] + \frac{1}{4S_U}\big[\mathbf{G}^*_D + S_U\mathbf{U}^*_D\big] \tag{5.3}$$

Once the strongly-interacting state is available, the electric and magnetic fields at the z-edge of the mesh can be found as follows

$$E^*_z = \tilde{\varepsilon}_{xz}D^*_x + \tilde{\varepsilon}_{yz}D^*_y + \tilde{\varepsilon}_{zz}D^*_z; \qquad H^*_z = \tilde{\mu}_{xz}B^*_x + \tilde{\mu}_{yz}B^*_y + \tilde{\mu}_{zz}B^*_z \tag{5.4}$$

These are the edge-centered fields from the strongly-interacting state of the MuSIC Riemann solver that are to be used in the curl-type updates shown in Fig. 1 and explicited in the next section. This completes our formal description of the MuSIC Riemann solver without sub-structure for CED with general permittivity and permeability tensors.

When the permittivity and permeability tensors are diagonal, a very substantial simplification of eqn. (5.4) can be obtained. Please note that the diagonal terms in the above-mentioned tensors can have different values, so the expressions we are about to derive have substantial utility. We are only interested in the z-components of the edge-collocated electric and magnetic field vectors. They can be written explicitly as follows

$$E^*_z = \frac{\tilde{\varepsilon}_{zz}}{4}(D_{z;RU} + D_{z;LU} + D_{z;LD} + D_{z;RD}) - \frac{\tilde{\varepsilon}_{zz}\tilde{\mu}_{xx}}{2S_U}\left[\frac{1}{2}(B_{x;RU} + B_{x;LU}) - \frac{1}{2}(B_{x;RD} + B_{x;LD})\right]$$
$$+ \frac{\tilde{\varepsilon}_{zz}\tilde{\mu}_{yy}}{2S_R}\left[\frac{1}{2}(B_{y;RU} + B_{y;RD}) - \frac{1}{2}(B_{y;LU} + B_{y;LD})\right] \tag{5.5}$$

and

$$H^*_z = \frac{\tilde{\mu}_{zz}}{4}(B_{z;RU} + B_{z;LU} + B_{z;LD} + B_{z;RD}) + \frac{\tilde{\mu}_{zz}\tilde{\varepsilon}_{xx}}{2S_U}\left[\frac{1}{2}(D_{x;RU} + D_{x;LU}) - \frac{1}{2}(D_{x;RD} + D_{x;LD})\right]$$
$$- \frac{\tilde{\mu}_{zz}\tilde{\varepsilon}_{yy}}{2S_R}\left[\frac{1}{2}(D_{y;RU} + D_{y;RD}) - \frac{1}{2}(D_{y;LU} + D_{y;LD})\right] \tag{5.6}$$

The above two equations can be defined at any z-edge of the mesh and are to be used in the curl-type update equations. Cyclic rotations with $(x, y, z) \rightarrow (y, z, x)$ and $(x, y, z) \rightarrow (z, x, y)$ can be applied to the above two formulae to give us the edge-collocated x- and y-components.

The first terms in the above two equations clearly show that the multidimensional Riemann solver gives us a centered electric and magnetic field that is the arithmetic average of the four fields coming together at that vertex. The remaining two terms in each of the above two equations give us the multidimensional dissipation. We see that the edge-collocated components of the electric and magnetic fields provided by the two-dimensional Riemann solver can be obtained entirely from the reconstructed magnetic induction vector and the reconstructed electric displacement vector. Section 4.2 of Balsara et al. [16] provides a detailed discussion of how these dissipation terms serve to stabilize a higher-order Godunov scheme. As the order of the reconstruction is improved, the dissipative contribution decreases for smooth variations in the field equations. As a result, with increasing order of accuracy, we get reduced dissipation when the primal variables are smoothly described on the mesh.

This completes our discussion of the multidimensional Riemann solver. This is the third step in a timestep loop for CED. The ADER scheme from the previous section is already capable of giving us the four space-centered and time-centered input variables that are needed to invoke the multidimensional Riemann solver at each edge, see Fig. 2. The MuSIC Riemann solver then gives us the multidimensionally upwinded edge-aligned components of the magnetic field and the electric field, see Fig. 1. These are the very variables that are needed for the time update that is described in eqns. (2.16) and (2.18). In fact, the update in eqns. (2.16) and (2.18) constitutes the fourth step in a timestep loop for CED.

6. Pointwise synopsis of the method at second order

We have indeed been describing the steps that go into a time–step loop for CED in Sections 3, 4 and 5. So in some sense, the algorithm described in the paper is implemented in the same sequence that the paper is written. Even so, it may help to catalogue the steps in the algorithm in one place so that the interested reader can see the whole picture.

We start out with the facially-collocated normal components of the electric displacement and the magnetic induction. The overarching goal is to find a way to update these variables on the mesh using eqns. (2.16) and (2.18), as shown in Fig. 1. This is accomplished with the following steps.

1) Starting with the facially-collocated normal components of the electric displacement and the magnetic induction, we carry out the constraint-preserving reconstruction for each of those two vector fields. For the electric displacement, the desired end result within each zone is a vector field given by eqns. (3.7), (3.8) and (3.9). For the magnetic induction, a completely analogous vector field can be specified within each zone. This is done by following the steps in Section 3.

2) We now have higher-order spatial derivatives within each zone for each of these two vector fields. The vector fields for the electric displacement and the magnetic induction satisfy their respective constraints in a global sense. We would like

to know how these vector fields evolve for a short interval of time (in-the-small evolution) within each zone in a fashion that is consistent with the conservation law in eqns. (2.11) and (2.12). This is done using the ADER predictor step described in Section 4. The ADER method at second order is based on eqns. (4.10) to (4.17). It can work with stiff or non-stiff source terms. The method is iterative and converges fast – within two or three iterations. If stiff source terms are present, the sub-iteration described in Sub-section 4.3 gives us a very fast solution method. The ADER method presented here is unconditionally stable and can handle source terms of any strength. The end result of this step is that it gives us the space–time representation (in the reference element for each zone) of the solution vector $\mathbf{u}(\xi, \eta, \zeta, \tau)$ in eqn. (4.3). The modes of the solution vector within each zone are worth saving because they will give us the inputs for the multidimensional Riemann solver. The ADER step also gives us space–time representations of the fluxes; eqns. (4.4), (4.5) and (4.6). While the space–time fluxes may be useful, we do not specifically save them in this implementation. The other important end result in this step is that we also get the space–time representation of the source terms $\mathbf{s}(\xi, \eta, \zeta, \tau)$. These source terms within each zone are worth saving because they give us the currents at the zone faces.

3) The previous ADER step has given us an in-the-small space–time representation of the primal variables within each zone. However, we are dealing with a hyperbolic system where all the zones interact with one another to yield the edge-collocated magnetic and electric fields shown in Fig. 1. The MuSIC Riemann solver, described in Section 5, mediates that interaction in a truly multidimensionally upwinded fashion. It is invoked at each edge of the mesh. It takes as its input the four space–time reconstructed values of the primal variables from the four zones that surround that edge, see Fig. 2. It produces as an output the edge-aligned components of the magnetic field and the electric field. When the material properties result in diagonal permittivity and permeability tensors, i.e. the usual case, eqns. (5.5) and (5.6) can be directly used to get those outputs. When the permittivity and permeability tensors are non-diagonal, eqns. (5.1) to (5.4) give us those desired outputs.

4) At each face of the mesh, we also want a high-order estimate of the current densities. Each face has two neighboring zones on either side of it. Since we have saved the space–time evolution of the source terms $\mathbf{s}(\xi, \eta, \zeta, \tau)$ within each zone, we can arithmetically average the appropriate source terms from the neighboring zones to the zone-face. This is done for all zone faces. This gives us the current densities at the faces. It does so in a way that respects the stiffness of the source terms.

5) We have now assembled all the terms that are needed in the update that is described in eqns. (2.16) and (2.18). Those updates are made, giving us a time-advanced version of our primal variables at each face of the mesh.

This completes our description of the time-update for CED using our new scheme that is based on three novel algorithmic developments reported in this paper. The advances are: **1)** constraint-preserving reconstruction; **2)** ADER predictor step that respects the sub-cell variation of the material properties and the stiffness in the source terms; **3)** Multidimensional upwinding given by the MuSIC Riemann solvers. Our new method has all the nice constraint-preserving properties of the FDTD methods, while also benefiting from our novel reformulations of all the desirable attributes of FVTD methods within the framework of higher-order Godunov schemes. In that sense, it represents a grand synthesis of FDTD and FVTD methods in CED, with the best attributes of both methods included in our present method. We have made all these advances within the context of second-order schemes, but in a sequel paper we will extend these advances to higher orders of accuracy.

7. Results

We present several stringent tests of our algorithm. The first test shows the native accuracy of the scheme. The next three tests concern the propagation of waves at dielectric interfaces with substantial variation in relative permittivity. The last two tests show the propagation of waves in conductors with very substantial variation in conductivity. In all instances, we used the second-order ADER-WENO scheme that we have presented in this paper.

It is also interesting to compare our second-order ADER scheme to a second-order Runge–Kutta scheme. Runge–Kutta schemes for PDEs have been described in Shu and Osher [44,45], Shu [46] and Spiteri and Ruuth [42,43]; for implicit–explicit SSP-RK methods, see Pareschi and Russo [40], Hunsdorfer and Ruuth [33] and Kupka et al. [37]. In this work, we used the IMEX-SSP2(3,2,2) stiffly-accurate scheme from Pareschi and Russo [40]. In Balsara et al. [16] we showed how these Runge–Kutta schemes can be adapted to treat stiff source terms in CED. Both the Runge–Kutta and the ADER schemes use the same reconstruction strategies and the same MuSIC Riemann solver for computational electrodynamics. The only difference is that during one time–step the ADER scheme requires one reconstruction step per zone, uses one predictor step per zone and invokes the Riemann solver once at each edge of the mesh. The Runge–Kutta scheme does not have a predictor step but rather carries out the update in two stages. We have to carry out one reconstruction step per zone for each of the two sub-stages in the Runge–Kutta algorithm. Likewise, we have to invoke the Riemann solver twice per time–step at each edge of the mesh.

7.1. Propagation of a plane electromagnetic wave in two dimensions

The three-dimensional version of this test has already been reported in Balsara et al. [16]. For that reason, in this paper, we display the two-dimensional version of this test problem. This test problem consists of a plane polarized electromagnetic wave propagating in a vacuum along the north–east diagonal of a two-dimensional Cartesian mesh spanning $[-0.5, 0.5] \times$

Table 1
This table shows the accuracy analysis for the second-order ADER-WENO scheme for the propagation of an electromagnetic wave in vacuum. A CFL of 0.45 was used. The errors and accuracy in the y-component of the electric displacement vector and z-component of the magnetic induction are shown.

Zones	D_y L_1 error	D_y L_1 accuracy	D_y L_{inf} error	D_y L_{inf} accuracy
16^2	4.0251E−05		6.2748E−05	
32^2	5.7988E−06	2.80	9.1293E−06	2.78
64^2	1.2316E−06	2.24	1.9344E−06	2.24
128^2	3.0299E−07	2.02	4.7586E−07	2.02

Zones	B_z L_1 error	B_z L_1 accuracy	B_z L_{inf} error	B_z L_{inf} accuracy
16^2	2.0025E−02		3.1079E−02	
32^2	2.8994E−03	2.79	4.5623E−03	2.77
64^2	6.2719E−04	2.21	9.8436E−04	2.21
128^2	1.5490E−04	2.02	2.4327E−04	2.02

Table 2
This table shows the accuracy analysis for the second-order RK-WENO scheme for the propagation of an electromagnetic wave in vacuum. A CFL of 0.45 was used. The errors and accuracy in the y-component of the electric displacement vector and z-component of the magnetic induction are shown.

Zones	D_y L_1 error	D_y L_1 accuracy	D_y L_{inf} error	D_y L_{inf} accuracy
16^2	3.2807E−04		5.0943E−04	
32^2	8.8783E−05	1.89	1.3947E−04	1.87
64^2	2.2671E−05	1.97	3.5602E−05	1.97
128^2	5.6986E−06	1.99	8.9518E−06	1.99

Zones	B_z L_1 error	B_z L_1 accuracy	B_z L_{inf} error	B_z L_{inf} accuracy
16^2	1.7247E−01		2.7021E−01	
32^2	4.7337E−02	1.87	7.4087E−02	1.87
64^2	1.2096E−02	1.97	1.8990E−02	1.96
128^2	3.0423E−03	1.99	4.7778E−03	1.99

$[−0.5, 0.5]$ meter. Periodic boundary conditions were enforced. The magnetic induction was initialized using a magnetic vector potential given by

$$\mathbf{A}(x, y, z, t) = \frac{1}{2\pi} \sin\left[2\pi(x + y - \sqrt{2}ct)\right]\hat{y} \tag{7.1}$$

and the components of the magnetic induction vector were obtained at the zone faces by using the relationship $\mathbf{B} = \nabla \times \mathbf{A}$. The electric displacement was initialized using an electric vector potential given by

$$\mathbf{C}(x, y, z, t) = -\frac{1}{2\pi\sqrt{2}} \sin\left[2\pi(x + y - \sqrt{2}ct)\right]\hat{z} \tag{7.2}$$

and the components of the electric displacement vector were obtained at the zone faces by using the relationship $\mathbf{D} = c\varepsilon_0(\nabla \times \mathbf{C})$ where c is the speed of light in free space and $\varepsilon_0 = 8.85 \times 10^{-12}$ F/m is the free space permittivity. With these analytical forms in hand, it is possible to evaluate the accuracy of the solution at any later time if it is set up correctly at the initial time on the mesh. For this EM field, we choose the wavelength to be 1 meter. The problem was run to a final time of 3.5 nano-second on the computational mesh.

Table 1 shows the accuracy analysis for the second order ADER-WENO scheme. It used the piecewise linear parts from a centered $r = 3$ WENO reconstruction. The errors and accuracy in the y-component of the electric displacement vector and z-component of the magnetic induction are shown at the last time point in the simulation. Table 2 shows the accuracy analysis for the second order RK-WENO scheme. For a description of implicit–explicit SSP-RK methods, see Pareschi and Russo [40], Hunsdorfer and Ruuth [33] and Kupka et al. [37]. As before, the errors and accuracy in the y-component of the electric displacement vector and z-component of the magnetic induction are shown at the last time point in the simulation. We ran these simulations with a CFL of 0.45. We see that the schemes meet their designed second-order accuracy. However, please notice two important facets that emerge from comparing the numbers in Tables 1 and 2. First, the ADER-WENO scheme reaches its design accuracy much faster. Second, the ADER-WENO scheme retains a substantial advantage in accuracy over the RK-WENO scheme on meshes with comparable resolution.

Table 3 shows the same result from the classical FDTD scheme. Because FDTD is completely symmetrical (in free space) between electric and magnetic variables, the accuracy of the magnetic variables would exactly track that of the electric variables. For that reason, we only show the data for the electric displacement vector field. We see that FDTD also meets its designed second order of accuracy. Furthermore, we see that the ADER-WENO scheme and classical FDTD show somewhat comparable levels of error in the L_1 norm. It is well-known that non-linear hybridization improves the phase accuracy of features that move on the mesh. For that reason, the ADER-WENO scheme, which is non-linearly hybridized, shows substantial improvement over the FDTD scheme in the L_∞ norm.

Table 3

This table shows the accuracy analysis for the classical, second-order FDTD scheme for the propagation of an electromagnetic wave in vacuum. A CFL of 0.5 was used. The errors and accuracy in the y-component of the electric displacement vector are shown. Because the FDTD scheme is completely symmetrical in magnetic and electric variables, the accuracy of the z-component of the magnetic induction would exactly track the accuracy of the electric displacement. For this reason, we do not show the accuracy for the magnetic induction.

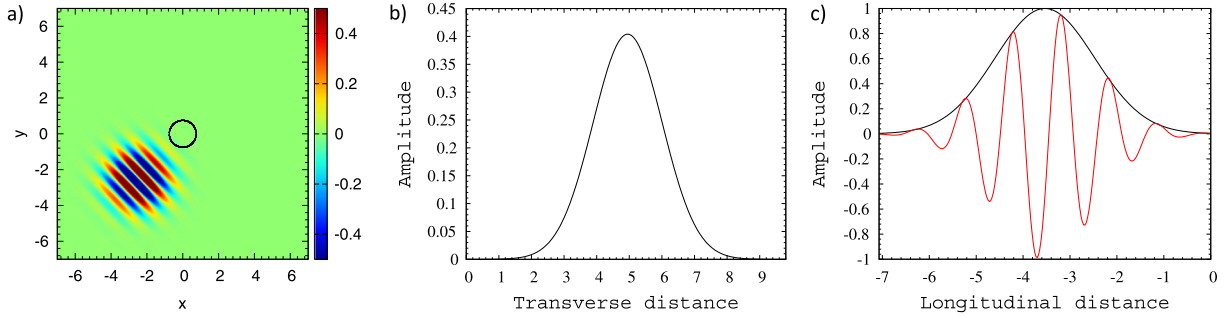| Zones	D_y L_1 error	D_y L_1 accuracy	D_y L_{inf} error	D_y L_{inf} accuracy
16^2	6.0337E−05		1.2404E−02	
32^2	1.7142E−05	1.82	3.0721E−03	2.01
64^2	4.4121E−06	1.96	7.6623E−04	2.00
128^2	1.1110E−06	1.99	1.9144E−04	2.00

Fig. 4. (a) is a visualization of the B_z field of the impinging compact pulse in the computational grid at the beginning of the simulation. The pulse propagates obliquely (at 45 degrees) on the mesh. (b) and (c) show, respectively, the Gaussian variation of the B_z field along transverse and longitudinal cuts through the compact pulse.

7.2. Compact Gaussian electromagnetic pulse incident on a refractive disk

This problem was slightly modified from Zakharian et al. [59] and concerns the scattering interaction of a compact electromagnetic pulse impinging upon a dielectric disk. The pulse was initialized with a Gaussian taper in both the transverse and longitudinal directions using magnetic and electric vector potentials given respectively by:

$$\mathbf{A}(x, y, z) = \frac{\lambda}{2\pi} \sin\left[\frac{2\pi}{\lambda}(x + y)\right] e^{-\frac{(x-a)^2 + (y-b)^2}{\chi^2}} \hat{y} \tag{7.3}$$

and

$$\mathbf{C}(x, y, z) = -\frac{\lambda}{2\pi\sqrt{2}} \sin\left[\frac{2\pi}{\lambda}(x + y)\right] e^{-\frac{(x-a)^2 + (y-b)^2}{\chi^2}} \hat{z} \tag{7.4}$$

Here, the components of the magnetic induction vector were calculated at the zone faces using $\mathbf{B} = \nabla \times \mathbf{A}$, and the components of the electric displacement vector were obtained at the zone faces using $\mathbf{D} = c\varepsilon_0(\nabla \times \mathbf{C})$. Numerical quadrature of sufficient accuracy was used at the edges of the mesh to evaluate the facially-collocated components of $\mathbf{B}$ and $\mathbf{D}$. We used $\lambda = 1.5$ m, $\chi = 1.5$ m and $(a, b) = (-2.5, -2.5)$ m to initialize $\mathbf{A}$ and $\mathbf{C}$ in two-dimensional rectangular computational grid spanning $[-7, 7] \times [-7, 7]$ m. The simulation was run to a time of 23.3 ns.

Fig. 4a is a visualization of the B_z field of the impinging compact pulse as it is initialized on the computational grid at the start of the simulation period. The pulse propagates obliquely (at 45 degrees) on the grid. Figs. 4b and 4c show, respectively, the Gaussian variation of the B_z field along transverse and longitudinal cuts through the compact pulse.

The compact electromagnetic pulse described above subsequently strikes a circular dielectric disk located at the center of the computational grid. The disk has a radius of 0.75 m, a permeability of $\mu_0 = 4\pi \times 10^{-7}$ N/A^2, and a relative permittivity given by:

$$\varepsilon_r(x, y, z) = 5.0 - 4.0 \tanh\left(\frac{\sqrt{x^2 + y^2} - 0.75}{0.08}\right) \tag{7.5}$$

Here, $\varepsilon_r = 9$ at the center of the disk and tapers rapidly to the ambient value of 1 at the outer edge of the disk. We used uniform meshes with varying number of zones so that the taper in the above-mentioned hyperbolic tangent function spans a larger number of zones on finer meshes. For example, on a uniform mesh with 180^2 zones, a taper of 0.08 m in the above equation corresponds to about one zone width.

Figs. 5a, 5b, and 5c show, respectively, B_z, D_x, and D_y at time 9.37 ns. Figs. 5d, 5e, and 5f show the same at time 23.3 ns. The perimeter of the dielectric disk is identified by the black circle. For the simulation shown in Fig. 5, we used a second-order-accurate scheme using a 720×720 zone mesh. We have also run this same simulation on a range of mesh
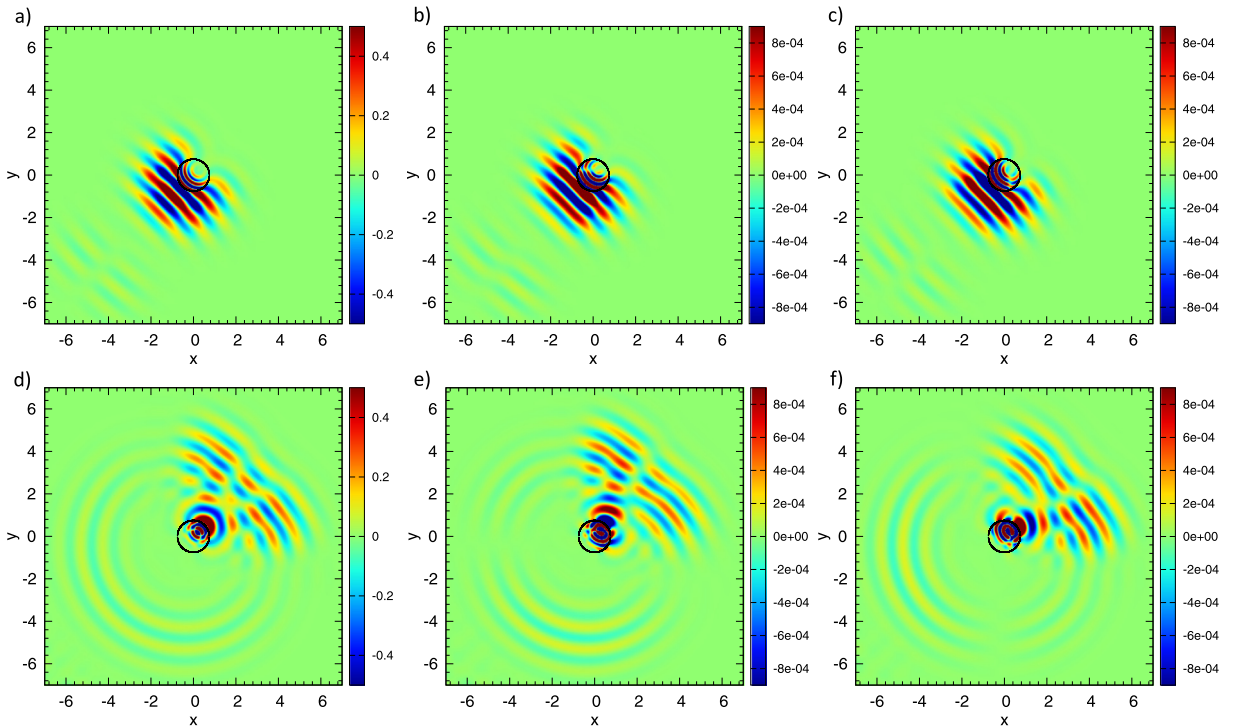
Fig. 5. (a), (b), and (c) visualize B_z, D_x, and D_y at time 9.36 ns. (d), (e), and (f) show the same at time 23.3 ns. The perimeter of the dielectric disk is identified by the black circle.

sizes and used mesh convergence to show that the method actually achieves the designed order of accuracy. Because an analytical solution is not available, we used a very large mesh with 2880^2 zones to calculate the reference solution. Table 4 shows the accuracy analysis for the second-order scheme for a range of mesh resolutions. We see that our second-order scheme achieves its designed accuracy.

The results from Runge–Kutta time-stepping are shown in Table 5. Comparing Tables 4 and 5, we see that the ADER time-stepping is four to five times more accurate than the Runge–Kutta time-stepping. Furthermore, because it can respond to sub-cell variations in the material properties, the ADER method reaches its design accuracy on a 720^2 zone mesh whereas the Runge–Kutta method seems to require a larger mesh to reach its design accuracy. However, both methods do reach their design accuracies.

In this problem, the permittivity varies by almost an order of magnitude. We see, therefore, that the ADER-based code is more adept at handling large variations in the material properties that might occur over one or two zones. The ADER-based method is also 66% more expensive per time–step than the Runge–Kutta-based method when the stiff source terms are implicitly updated in each zone. (For this problem, of course, the source terms are not present and the update speeds are comparable.) However, as in the previous test problem, the ADER-WENO scheme achieves its design accuracy on smaller meshes than the RK-WENO scheme. Furthermore, the ADER-WENO scheme provides a more accurate result than the RK-WENO scheme when meshes of comparable resolution are used.

The ADER versus Runge–Kutta results that are reported here are specific to second order. It is possible that at higher orders the higher quality reconstruction might close the accuracy gap between the two time-stepping paradigms. This is an interesting topic of future research.

7.3. Refraction of a compact electromagnetic beam by a dielectric slab

The problem is set up on a rectangular xy-domain that spans $[-5, 8] \times [-2.5, 7]$ μm. For the simulation shown, we use a second-order-accurate scheme using a 1300×950 zone mesh. A dielectric slab having a permeability of μ_0 and permittivity of ε is modeled such that ε is given by

$$\varepsilon(x, y, z) = 1.625\varepsilon_0 + 0.625\varepsilon_0 \tanh\left(\frac{x}{10^{-8}}\right), \tag{7.6}$$

where, ε_0 is the free space permittivity. Here, ε is chosen such that it has a value of $2.25\varepsilon_0$ for $x \geq 0$ and tapers rapidly to the ambient value of ε_0 for $x < 0$.

The magnetic induction was initialized using a magnetic vector potential given by

Table 4
This table shows the accuracy analysis for the second-order scheme with ADER timestepping for the propagation of a Gaussian pulse of radiation that is incident on a refractive disk. A CFL of 0.45 was used. The errors and accuracy in the y-component of the electric displacement vector and z-component of the magnetic induction are shown.

Zones	D_y L_1 error	D_y L_1 accuracy	D_y L_{inf} error	D_y L_{inf} accuracy
180^2	3.3227E−05		2.0611E−02	
360^2	1.4396E−05	1.21	9.6259E−03	1.10
720^2	3.3079E−06	2.12	2.2001E−03	2.13
1440^2	5.9909E−07	2.47	4.0498E−04	2.44

Zones	B_z L_1 error	B_z L_1 accuracy	B_z L_{inf} error	B_z L_{inf} accuracy
180^2	1.2178E−02		3.5801E+00	
360^2	5.1596E−03	1.24	1.6888E+00	1.08
720^2	1.1818E−03	2.13	3.6701E−01	2.20
1440^2	2.1408E−04	2.46	6.4952E−02	2.50

Table 5
This table shows the accuracy analysis for the second-order scheme with Runge–Kutta time-stepping for the propagation of a Gaussian pulse of radiation that is incident on a refractive disk. A CFL of 0.45 was used. The errors and accuracy in the y-component of the electric displacement vector and z-component of the magnetic induction are shown.

Zones	D_y L_1 error	D_y L_1 accuracy	D_y L_{inf} error	D_y L_{inf} accuracy
180^2	6.2097E−05		2.1167E−02	
360^2	3.3412E−05	0.89	1.5553E−02	0.44
720^2	1.0626E−05	1.65	5.7303E−03	1.44
1440^2	2.6146E−06	2.02	1.4605E−03	1.97

Zones	B_z L_1 error	B_z L_1 accuracy	B_z L_{inf} error	B_z L_{inf} accuracy
180^2	2.7652E−02		3.6734E+00	
360^2	1.3262E−02	1.06	2.6027E+00	0.50
720^2	4.0789E−03	1.70	8.9640E−01	1.54
1440^2	1.0160E−03	2.01	2.4597E−01	1.87

$$\mathbf{A}(x, y, z, t) = \frac{0.25\lambda}{2\pi} \sin\left[\frac{2\pi}{\lambda}(x + y - \sqrt{2}ct)\right]\left[1 - \tanh\left(\frac{\text{SIGN}(1, \frac{y-x}{\sqrt{2}})(\frac{y-x}{\sqrt{2}} - \text{SIGN}(1, \frac{y-x}{\sqrt{2}})d)}{\delta}\right)\right]$$
$$\left[1 - \tanh\left(\frac{(x-a) + (y-b) - \sqrt{2}ct}{0.1\lambda}\right)\right]\hat{y} \tag{7.7}$$

and the components of the magnetic induction vector at time $t = 0$ were obtained at the zone faces by using the relationship $\mathbf{B} = \nabla \times \mathbf{A}$. Numerical quadrature of sufficient accuracy was used at the edges of the mesh to evaluate the facially-collocated components of the magnetic induction. The SIGN function in the above equation is the same function that is standard in the Fortran language, so that the formulae given can be directly implemented in a code. The electric displacement was initialized using an electric vector potential given by

$$\mathbf{C}(x, y, z, t) = -\frac{0.25\lambda}{2\pi\sqrt{2}} \sin\left[\frac{2\pi}{\lambda}(x + y - \sqrt{2}ct)\right]\left[1 - \tanh\left(\frac{\text{SIGN}(1, \frac{y-x}{\sqrt{2}})(\frac{y-x}{\sqrt{2}} - \text{SIGN}(1, \frac{y-x}{\sqrt{2}})d)}{\delta}\right)\right]$$
$$\left[1 - \tanh\left(\frac{(x-a) + (y-b) - \sqrt{2}ct}{0.1\lambda}\right)\right]\hat{z} \tag{7.8}$$

The components of the electric displacement vector at time $t = 0$ were obtained at the zone faces by using the relationship $\mathbf{D} = c\varepsilon_0(\nabla \times \mathbf{C})$. As before, numerical quadrature of sufficient accuracy was used at the edges of the mesh to evaluate the facially-collocated components of the electric displacement. We used $\lambda = 0.5$ μm, $d = 2.5\lambda$, $\delta = 0.5\lambda$ and $(a, b) = (-3.0\lambda, -3.0\lambda)$ to set up the compact electromagnetic beam. The simulation was run to a time of 4.0×10^{-14} s. For this two-dimensional simulation, we use an inflow boundary condition on the left half of lower y-boundary and an outflow boundary condition for all other boundaries. We assign the time-dependent values of the facially-collocated components of electric displacement and magnetic induction in the ghost zones of the inflowing boundary using the above mentioned time-dependent vector potentials. This enables the wave to smoothly flow into the computational domain.

Figs. 6a, 6b, and 6c show, respectively, B_z, D_x, and D_y at the initial time. Figs. 6d, 6e, and 6f show the same at the final time. The surface of the dielectric slab is shown by a vertical black line. (In other words, the vertical black line shows the midpoint in the taper that is used for ε.) The inclined black lines show the angles of incidence, refraction and reflection and these black lines are over-plotted on the field components to guide our eye. The impinging beam of radiation is incident on the surface of the dielectric slab at an angle of 45°. Thus, according to Snell's law, the angle of refraction should be 28.12° since the refractive index of the dielectric slab is 1.5. We also observe that some of the radiation is reflected from
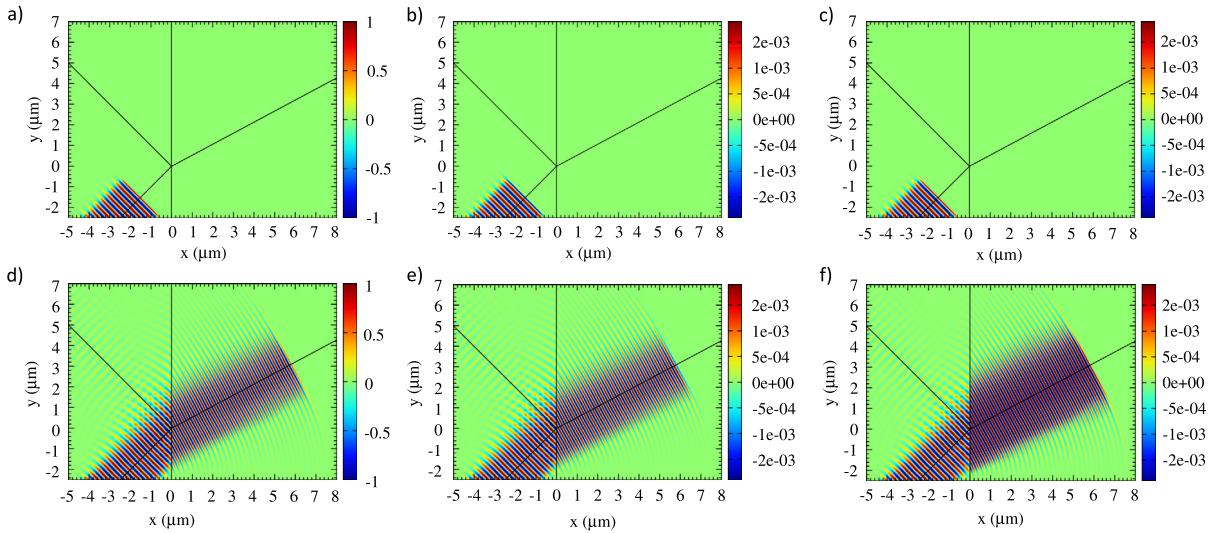
Fig. 6. (a), (b), and (c) visualize B_z, D_x, and D_y at the initial time. (d), (e), and (f) show the same at a final time of 4×10^{-14} s. The surface of the dielectric slab is identified by the vertical black line. The oblique black lines demarcate the angle of incidence, the angle of refraction and the angle of reflection.

the surface of the slab. The presence of a reflected wave is consistent with the Fresnel conditions for transmission and reflection of radiation at dielectric interfaces.

7.4. Total internal reflection of a compact electromagnetic beam by a dielectric slab

This problem is set up on a rectangular xy-domain that spans $[-6, 1] \times [-2.5, 6]$ µm. For the simulation shown, we use a second-order-accurate scheme using a 700×850 zone mesh. A dielectric slab having a permeability of μ_0 and permittivity of ε is modeled such that ε is given by

$$\varepsilon(x, y, z) = 2.5\varepsilon_0 - 1.5\varepsilon_0 \tanh\left(\frac{x}{2.5 \times 10^{-9}}\right), \tag{7.9}$$

where, ε_0 is the free space permittivity. Here, ε is chosen such that it has a value of $4.0\varepsilon_0$ for $x \leq 0$ and tapers rapidly to the ambient value of ε_0 for $x > 0$. This value of permittivity for $x < 0$ implies a refractive index of 2 for the dielectric slab. For such slab, the critical angle for total internal reflection is $30°$.

The magnetic induction and electric displacement were initialized using eqns. (7.7) and (7.8), respectively and similar procedures as previous sub-section were used to evaluate the facially-collocated components of the field vectors. However, for this problem, we used a wave of frequency 5.0×10^{14} Hz which gives $\lambda = 0.3$ µm inside the dielectric slab. Also, $d = 2.5\lambda$, $\delta = 0.5\lambda$ and $(a, b) = (-3.0\lambda, -3.0\lambda)$ were used to set up the compact electromagnetic beam. The simulation was run to a time of 5.0×10^{-14} s. For this two-dimensional simulation, we use an inflow boundary condition on the lower y-boundary and an outflow boundary condition for all other boundaries. We assign the time-dependent values of the facially-collocated components of electric displacement and magnetic induction in the ghost zones of the inflowing boundary using the above mentioned time-dependent vector potentials.

Figs. 7a, 7b, and 7c show, respectively, B_z, D_x, and D_y at the initial time. Figs. 7d, 7e, and 7f show the same at the final time. The surface of the dielectric slab is shown by a vertical black line. (In other words, the vertical black line shows the midpoint in the taper that is used for ε.) The inclined black lines for the incident and reflected rays are over-plotted on the field components to guide our eye. The impinging beam of radiation is incident on the surface of the dielectric slab at an angle of $45°$. Thus, the incident angle is more than the critical angle for this material and hence, we see total internal reflection of the incident beam.

7.5. Compact electromagnetic beam impinging on a conducting slab

The purpose of this simulation is to show the performance of our algorithm when handling a conductor with a finite skin depth. We realize that a perfect electrical conductor (PEC) surface in CED would be treated differently. However, it is interesting to show how the code behaves when a compact electromagnetic beam impinges on a planar conducting slab with a finite but very large conductivity. From Huygen's principle, we of course expect most of the incident radiation to be reflected.

The problem is set up on a rectangular xy-domain that spans $[-25, 5] \times [-40, 40]$ m. For the simulations shown, we use a second-order-accurate scheme using a 1500×4000 zone mesh. A conducting slab having permittivity of ε_0 and permeability of μ_0 is modeled for $x \geq 0$ such that the conductivity σ is given by
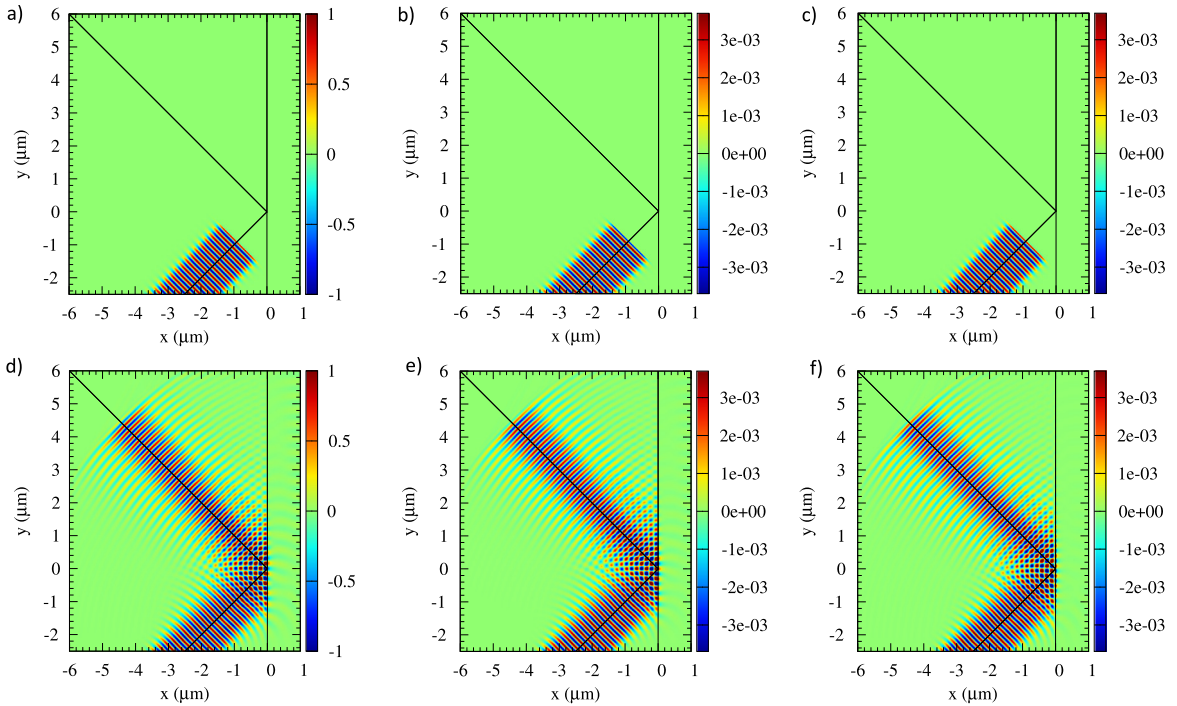
Fig. 7. (a), (b), and (c) visualize B_z, D_x, and D_y at the initial time. (d), (e), and (f) show the same at final time of 5×10^{-14} s. The surface of the dielectric slab is identified by the vertical black line. The oblique black lines demarcate the angle of incidence and the angle of total internal reflection.

$$\sigma(x, y, z) = \frac{\sigma_0}{2}\big(1.0 + \tanh(x/\Delta)\big) \tag{7.10}$$

Here, the conductivity goes from zero for $x < 0$ to σ_0 over a single zone.

The magnetic induction and electric displacement were initialized using Eqs. (7.7) and (7.8), respectively and similar procedures as previous two sub-sections were used to evaluate the facially-collocated components of the field vectors. However, for this problem, we used $\lambda = 2$ m, $d = 4\lambda$, $\delta = \lambda$ and $(a, b) = (-7.5\lambda, -7.5\lambda)$ to set up the compact electromagnetic beam. The simulation was run to a time of 1.83×10^{-7} s. For this two-dimensional simulation, we use an inflow boundary condition on the lower half of left x-boundary and an outflow boundary condition for all other boundaries. We assign the time-dependent values of the facially-collocated components of electric displacement and magnetic induction in the ghost zones of the inflowing boundary using the above mentioned time-dependent vector potentials.

We present results for the simulation run with conductivity of $\sigma_0 = 5.9 \times 10^7$ S/m which corresponds to the conductivity of copper, and hyperbolic tangent taper width of $\Delta = 0.0125\lambda$ which corresponds to slightly more than one-zone width. Figs. 8a, 8b, and 8c show, respectively, B_z, D_x, and D_y at the initial time. Figs. 8d, 8e, and 8f show the same at the final time of 1.83×10^{-7} s. The surface of the conducting slab is shown by a black line. (In other words, the black line shows the midpoint in the taper that is used for σ.)

Since the beam has a finite width, we see a small amount of spreading of the beam in the transverse direction because of diffraction. This is inevitable. However, it is interesting to see that with very reasonable resolutions, most of the incident intensity in the radiation is reflected back. Fig. 9 shows the interference pattern that develops between the incident and reflected radiation. Decreasing the taper Δ on a larger mesh would have increased the intensity of the reflected radiation. Likewise, increasing the conductivity σ_0 would also have increased the reflected intensity, while decreasing the skin depth. (For the meshes used here, we are unable to resolve the skin depth, but do please see the next problem.) Please also note that the method did not require any reduction of the time–step due to the very stiff source terms. Happily, the taper width can be restricted to a zone or two, with the result that the loss of resolution is not substantial, especially when adaptive mesh refinement is used.

7.6. Decay of a sinusoidal wave inside a conductor

The previous problem did not resolve the skin depth of the conductor. In this problem we do that and show that the numerical results accurately match the analytic results even when the skin depth is resolved with no more than ten zones. We use this one-dimensional problem to study the decay of sinusoidal plane wave propagating inside a conductor. For a good conductor, the conductivity $\sigma \gg 1$ and the amplitude of a sinusoidal wave propagating through such a conductor decays exponentially. Using this test problem, we test the performance of our code to verify whether the theoretical decay rate is actually captured by our code.
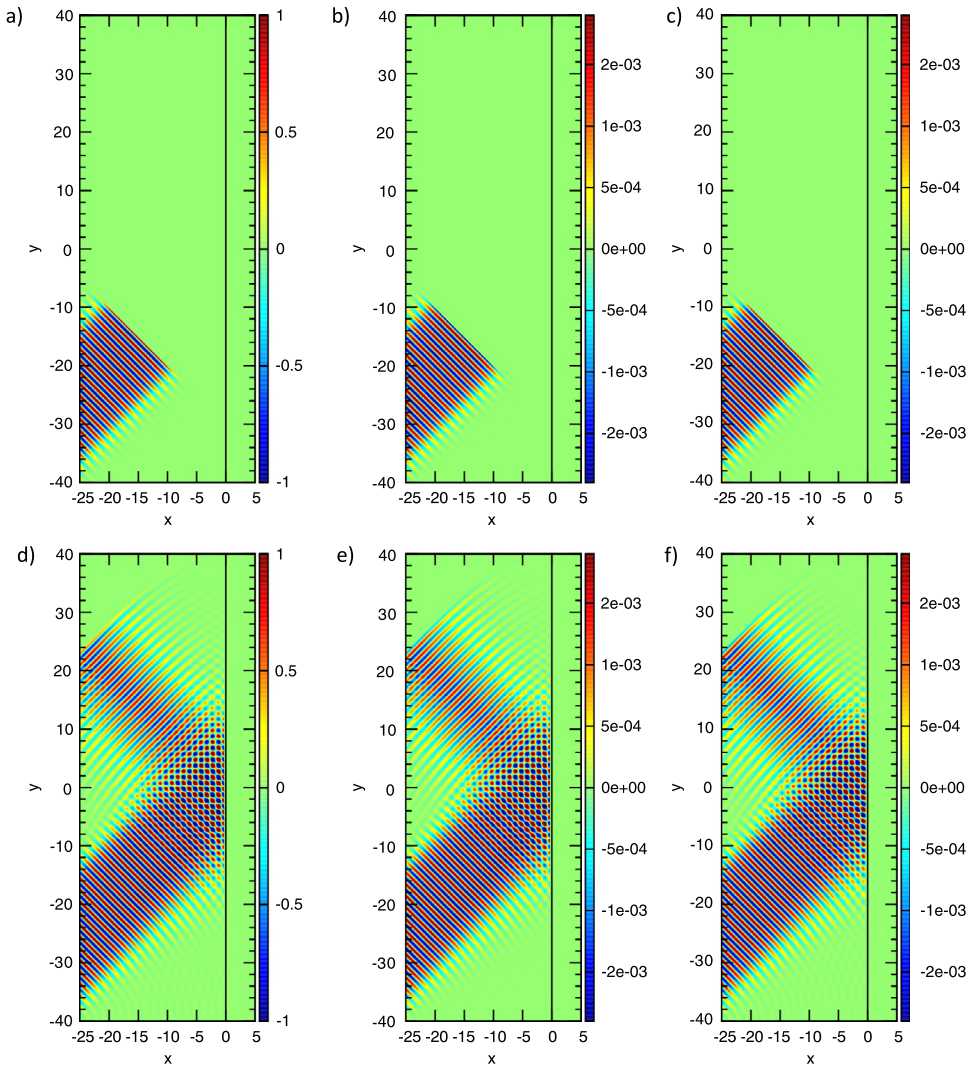
Fig. 8. (a), (b) and (c) show the initial configuration of B_z, D_x and D_y for the test problem where a beam of radiation is incident upon a conductor at $45°$. (d), (e) and (f) show the same variables at the final time of 1.83×10^{-7} s when the beam has reflected off the surface of the conductor. The conductor is located at $x = 0$ in the figure and is shown by a black line.

The problem is set up on a 1D domain that spans $[0, 10\delta]$ where δ is the skin depth of the conductor. For the simulations shown, we use a second-order-accurate scheme using a 100 zone mesh. Thus, we use 10 zones per skin depth for this simulation. Below we provide the analytical equations for a plane sinusoidal wave propagating in the positive x-direction inside the conducting material having permittivity of ε_0, permeability of μ_0 and conductivity σ. The magnetic induction vector is given by,

$$\mathbf{B}(x, y, z, t) = \exp\left(-\sqrt{r} \sin\left(\frac{\phi}{2}\right)x\right) \cos\left(\sqrt{r} \cos\left(\frac{\phi}{2}\right)x - \omega t\right)\hat{z} \tag{7.11}$$

and the electric displacement vector is given by,

$$\mathbf{D}(x, y, z, t) = \frac{\omega \varepsilon_0}{\sqrt{r}} \exp\left(-\sqrt{r} \sin\left(\frac{\phi}{2}\right)x\right) \cos\left(\sqrt{r} \cos\left(\frac{\phi}{2}\right)x - \omega t - \frac{\phi}{2}\right)\hat{y} \tag{7.12}$$

Here, $r = \sqrt{(\mu_0 \varepsilon_0 \omega^2)^2 + (\sigma \mu_0 \omega)^2}$ and $\phi = \tan^{-1}(\frac{\sigma}{\varepsilon_0 \omega})$, with ω being the angular frequency of the plane wave. Here ω is given by $\omega = 2\pi\nu$, and ν is the frequency of the wave measured in Hz. As before, numerical quadrature of sufficient accuracy was used at the faces of the mesh to evaluate the facially-collocated components of the field vectors. As can be seen from Eqs, (7.11) and (7.12), the skin depth for this material is given by $\delta = \frac{1}{\sqrt{r} \sin(\frac{\phi}{2})}$. The analytical form of the incoming wave (along with its time-dependence and its exponential taper) was initialized on the faces of the mesh in the four ghost zones to the left of the active computational domain. We used an outflow boundary condition at the right x-boundary.
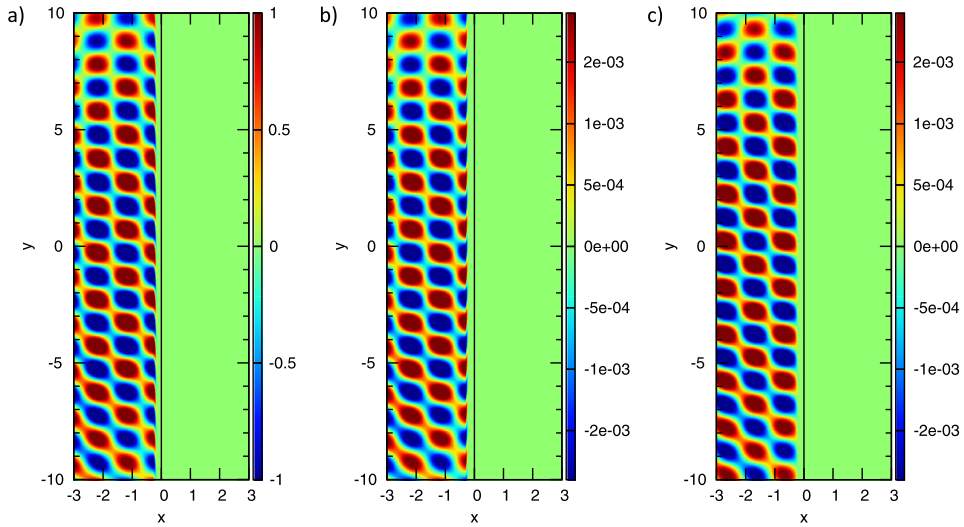
Fig. 9. (a), (b) and (c) show a zoom-in of Fig. 8(d), 8(e) and 8(f) and these figures are centered on the reflection region, spanning the sub-domain $[-3, 3] \times [-10, 10]$ m. The location of the midpoint in the taper for the conductivity is again shown by a black line.
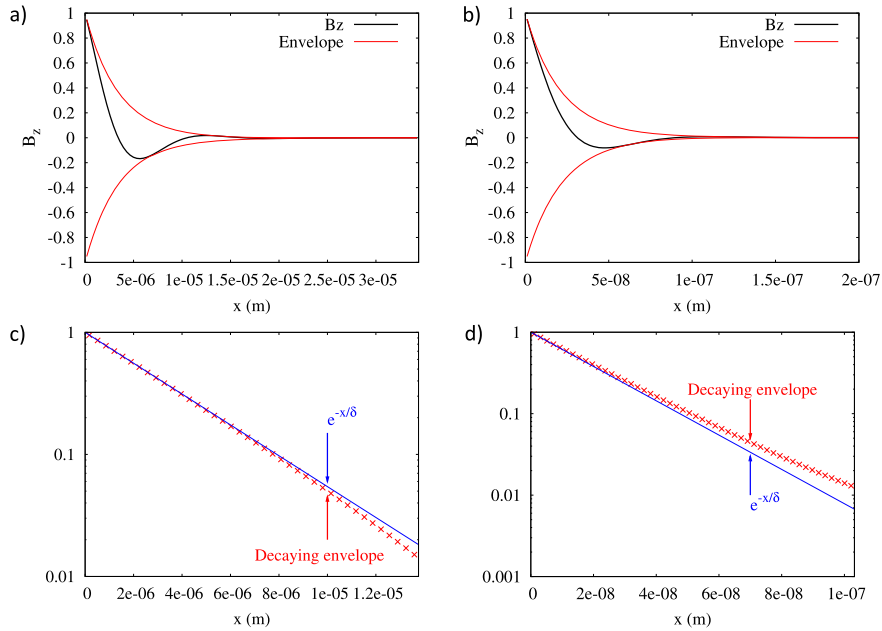

Fig. 10. (a) and (b) show the radial variations of B_z (black lines) and the decaying envelopes (red lines) inside carbon and copper, respectively. (c) and (d) present the structure of the numerically-obtained envelopes (red crosses) and the analytical envelopes (blue curve) on a semi-log scale for carbon and copper, respectively. (For interpretation of the references to color in this figure legend, the reader is referred to the web version of this article.)

Two simulations were carried out. In our first simulation we used a conductivity of $\sigma = 2.0 \times 10^3$ S/m which corresponds to the conductivity of amorphous carbon. In our second simulation we used $\sigma = 5.9 \times 10^7$ S/m which corresponds to the conductivity of copper. For carbon, we choose $\nu = 1.679 \times 10^{13}$ Hz which gives $\delta = 3.44 \times 10^{-6}$ m and a wavelength of the plane wave as $\lambda = 1.38 \times 10^{-5}$ m inside this material. We stop this simulation at a time of 2.38×10^{-13} s. For copper, we choose $\nu = 1.0 \times 10^{13}$ Hz which gives $\delta = 2.06 \times 10^{-8}$ m and a wavelength of the plane wave as $\lambda = 1.3 \times 10^{-7}$ m inside this material. We stop this simulation at a time of 2.0×10^{-13} s. Figs. 10a and 10b show the variations of B_z with radial distance inside carbon and copper, respectively. The exponentially decaying envelopes are also over-plotted. In Figs. 10c and 10d, we present the structure of the numerical envelopes (red crosses) and the analytical envelopes (blue curve) on a semi-log scale for carbon and copper, respectively. The numerically-obtained envelopes match quite well with the analytical envelopes. We have also carried out further tests (not reported here) that show that a substantially better match-up is obtained between simulated and the theoretical results if we use more than 10 zones per skin-depth.

8. Conclusions

FDTD and FVTD schemes for CED have evolved independently for a while. FDTD does not use reconstruction strategies or Riemann solvers. However, via an exact representation of the curl-type equations on a Yee mesh, it preserves the divergence constraints. FVTD methods do use reconstruction strategies as well as Riemann solvers. However, at least in the past, they have used zone-centered collocations. The zone-centered collocation precludes a preservation of the divergence constraints. In this paper we have made an important synthesis of the two methods so that the best advantages of FDTD and FVTD schemes are retained in the method presented here. The schemes we present use a staggered mesh formulation, resulting in an exact preservation of the constraints, just like FDTD schemes. However, they use the reconstruction strategies and Riemann solvers (after substantial modification and innovation) so that they retain the phase accuracy and gracious dissipation of the smallest-scale waves that are some of the better attributes of the FVTD schemes. Like all FVTD schemes, our methods extend seamlessly to higher orders, as will be shown in a subsequent paper.

Three advances are reported here that make our novel method especially well-adapted to the needs of the CED community. First, instead of using two staggered control volumes for the discretization of Ampere's and Faraday's laws, as is done in FDTD, we use the same control volume for both the curl-type equations, see Fig. 1. As a result, the primal variables in our scheme are the facially-collocated normal components of the electric displacement and the magnetic induction vector fields. A special type of globally constraint-preserving reconstruction is developed and presented in Section 3 for those vector fields, which enables the specification of the electric displacement vector field and the magnetic induction vector field at all points on the mesh. Second, a special type of ADER scheme is reported in Section 4 that permits close and efficient coupling between the flux and stiff source terms; i.e. high conductivities. Our ADER scheme also makes allowance for sub-cell variations in material properties; i.e. permittivity and permeability. After the ADER predictor step is evaluated, we can supply the input variables for the multidimensional Riemann solver at any time-point in the course of a time–step evolution. The ADER predictor step is not a crucial part of the method, however, and we show that a Runge–Kutta strategy will also perform quite well. The update of the face-centered electric displacement using Ampere's law requires edge-centered magnetic field components. Likewise, the update of the face-centered magnetic induction using Faraday's law requires edge-centered electric field components (Fig. 1). The third advance, reported in Section 5, consists of realizing that the edge-centered magnetic and electric fields can be provided by the MuSIC Riemann solver. Section 6 provides a synopsis of the method that is useful for implementation.

Several results are reported in Section 7 showing that the method works well. Indeed, it retains second-order accuracy even on problems which have almost an order-of-magnitude variation in the permittivity within one or two zones. Because our ADER-based predictor step is unconditionally stable in the presence of stiff source terms, our method can also handle near-infinite variations in the conductivity across one or two zones without any degradation in the time–step. This can be very useful in treating metallic surfaces where the effect of finite skin depth needs to be retained in the calculation. In general, the ADER-based code is more accurate at resolving sub-cell variations in the permeability and permittivity than the Runge–Kutta based code. However, the Runge–Kutta based code is slightly faster and easier to implement.

Acknowledgements

Appendix A

We consider the case where the permittivity and permeability matrices are diagonal in this Appendix. The matrix of right eigenvectors in the x-direction, with the eigenvectors arranged in columns having the same ordering as (2.13), is given by

$$
\mathbf{R}^x = \begin{pmatrix}
0 & 0 & 1 & 0 & 0 & 0 \\
-\sqrt{\dfrac{\tilde{\mu}_{zz}}{\tilde{\varepsilon}_{yy}}} & 0 & 0 & 0 & 0 & \sqrt{\dfrac{\tilde{\mu}_{zz}}{\tilde{\varepsilon}_{yy}}} \\
0 & \sqrt{\dfrac{\tilde{\mu}_{yy}}{\tilde{\varepsilon}_{zz}}} & 0 & 0 & -\sqrt{\dfrac{\tilde{\mu}_{yy}}{\tilde{\varepsilon}_{zz}}} & 0 \\
0 & 0 & 0 & 1 & 0 & 0 \\
0 & 1 & 0 & 0 & 1 & 0 \\
1 & 0 & 0 & 0 & 0 & 1
\end{pmatrix}
\tag{A.1}
$$

The corresponding matrix of left eigenvectors in the x-direction, with the eigenvectors arranged as rows having the same ordering as (2.13), is given by

$$\mathbf{L}^x = \begin{pmatrix} 0 & -\frac{1}{2}\sqrt{\frac{\tilde{\varepsilon}_{yy}}{\tilde{\mu}_{zz}}} & 0 & 0 & 0 & \frac{1}{2} \\ 0 & 0 & \frac{1}{2}\sqrt{\frac{\tilde{\varepsilon}_{zz}}{\tilde{\mu}_{yy}}} & 0 & \frac{1}{2} & 0 \\ 1 & 0 & 0 & 0 & 0 & 0 \\ 0 & 0 & 0 & 1 & 0 & 0 \\ 0 & 0 & -\frac{1}{2}\sqrt{\frac{\tilde{\varepsilon}_{zz}}{\tilde{\mu}_{yy}}} & 0 & \frac{1}{2} & 0 \\ 0 & \frac{1}{2}\sqrt{\frac{\tilde{\varepsilon}_{yy}}{\tilde{\mu}_{zz}}} & 0 & 0 & 0 & \frac{1}{2} \end{pmatrix} \tag{A.2}$$

The matrix of right eigenvectors in the y-direction, with the eigenvectors arranged in columns having the same ordering as (2.14), is given by

$$\mathbf{R}^y = \begin{pmatrix} \sqrt{\frac{\tilde{\mu}_{zz}}{\tilde{\varepsilon}_{xx}}} & 0 & 0 & 0 & 0 & -\sqrt{\frac{\tilde{\mu}_{zz}}{\tilde{\varepsilon}_{xx}}} \\ 0 & 0 & 1 & 0 & 0 & 0 \\ 0 & -\sqrt{\frac{\tilde{\mu}_{xx}}{\tilde{\varepsilon}_{zz}}} & 0 & 0 & \sqrt{\frac{\tilde{\mu}_{xx}}{\tilde{\varepsilon}_{zz}}} & 0 \\ 0 & 1 & 0 & 0 & 1 & 0 \\ 0 & 0 & 0 & 1 & 0 & 0 \\ 1 & 0 & 0 & 0 & 0 & 1 \end{pmatrix} \tag{A.3}$$

The corresponding matrix of left eigenvectors in the y-direction, with the eigenvectors arranged as rows having the same ordering as (2.14), is given by

$$\mathbf{L}^y = \begin{pmatrix} \frac{1}{2}\sqrt{\frac{\tilde{\varepsilon}_{xx}}{\tilde{\mu}_{zz}}} & 0 & 0 & 0 & 0 & \frac{1}{2} \\ 0 & 0 & -\frac{1}{2}\sqrt{\frac{\tilde{\varepsilon}_{zz}}{\tilde{\mu}_{xx}}} & \frac{1}{2} & 0 & 0 \\ 0 & 1 & 0 & 0 & 0 & 0 \\ 0 & 0 & 0 & 0 & 1 & 0 \\ 0 & 0 & \frac{1}{2}\sqrt{\frac{\tilde{\varepsilon}_{zz}}{\tilde{\mu}_{xx}}} & \frac{1}{2} & 0 & 0 \\ -\frac{1}{2}\sqrt{\frac{\tilde{\varepsilon}_{xx}}{\tilde{\mu}_{zz}}} & 0 & 0 & 0 & 0 & \frac{1}{2} \end{pmatrix} \tag{A.4}$$

Appendix B

We consider the case where the permittivity or permeability matrices have off-diagonal elements in this Appendix. The eigenvalues in eqn. (2.15) are so designed that we smoothly retrieve the limit in eqn. (2.13) when the permittivity and permeability become diagonal tensors. We can, therefore, design eigenvectors that smoothly retrieve the eigenvectors in eqns. (A.1) and (A.2). Let l_1^x and r_1^x denote the left and right eigenvectors corresponding to $\lambda_1^x = -\sqrt{\tau^x + \chi^x\sqrt{\kappa^x}}/\sqrt{2}$. I.e., λ_1^x is the first eigenvalue in the diagonal matrix $\mathbf{\Lambda}^x$, and so on. We formally write l_1^x and r_1^x in a form that could retrieve the eigenvectors in eqns. (A.1) and (A.2) as

$$\begin{aligned} r_1^x &= \begin{pmatrix} 0, & x_2, & x_3, & 0, & x_5, & 1 \end{pmatrix}^T \\ l_1^x &= \begin{pmatrix} y_1, & y_2, & y_3, & y_4, & y_5, & \frac{1}{2} \end{pmatrix} \end{aligned} \tag{B.1}$$

Here x_2, x_3 and x_5 are temporary variables that are evaluated by the following stack of equations

$$\begin{aligned} x_5 &= \frac{\tilde{\varepsilon}_{zz}\tilde{\mu}_{yz} - \tilde{\varepsilon}_{yz}\tilde{\mu}_{zz}}{(\lambda_1^x)^2 + \tilde{\varepsilon}_{yz}\tilde{\mu}_{yz} - \tilde{\varepsilon}_{zz}\tilde{\mu}_{yy}}; \\ x_2 &= \frac{1}{\lambda_1^x}(\tilde{\mu}_{yz}x_5 + \tilde{\mu}_{zz}); \qquad x_3 = -\frac{1}{\lambda_1^x}(\tilde{\mu}_{yy}x_5 + \tilde{\mu}_{yz}) \end{aligned} \tag{B.2}$$

Similarly, y_1 through y_5 are temporary variables that are evaluated by the following stack of equations

$$\begin{aligned} y_5 &= \frac{\tilde{\varepsilon}_{yy}\tilde{\mu}_{yz} - \tilde{\varepsilon}_{yz}\tilde{\mu}_{yy}}{2((\lambda_1^x)^2 + \tilde{\varepsilon}_{yz}\tilde{\mu}_{yz} - \tilde{\varepsilon}_{zz}\tilde{\mu}_{yy})}; \\ y_1 &= -\frac{1}{\lambda_1^x}(\tilde{\varepsilon}_{xz}y_5 - \tilde{\varepsilon}_{xy}/2); \qquad y_2 = -\frac{1}{\lambda_1^x}(\tilde{\varepsilon}_{yz}y_5 - \tilde{\varepsilon}_{yy}/2); \qquad y_3 = -\frac{1}{\lambda_1^x}(\tilde{\varepsilon}_{zz}y_5 - \tilde{\varepsilon}_{yz}/2); \\ y_4 &= \frac{1}{\lambda_1^x}(\tilde{\mu}_{xz}y_2 - \tilde{\mu}_{xy}y_3) \end{aligned} \tag{B.3}$$

Let l_2^x and r_2^x denote the left and right eigenvectors corresponding to $\lambda_2^x = -\sqrt{\tau^x - \chi^x \sqrt{\kappa^x}}/\sqrt{2}$. We formally write l_2^x and r_2^x in a form that could retrieve the eigenvectors in eqns. (A.1) and (A.2) as

$$r_2^x = \begin{pmatrix} 0, & x_2, & x_3, & 0, & 1, & x_6 \end{pmatrix}^T$$
$$l_2^x = \begin{pmatrix} y_1, & y_2, & y_3, & y_4, & \frac{1}{2}, & y_6 \end{pmatrix}$$

(B.4)

Here x_2, x_3 and x_6 are temporary variables that are evaluated by the following stack of equations

$$x_6 = \frac{\tilde{\varepsilon}_{yy}\tilde{\mu}_{yz} - \tilde{\varepsilon}_{yz}\tilde{\mu}_{yy}}{(\lambda_2^x)^2 + \tilde{\varepsilon}_{yz}\tilde{\mu}_{yz} - \tilde{\varepsilon}_{yy}\tilde{\mu}_{zz}};$$
$$x_2 = \frac{1}{\lambda_2^x}(\tilde{\mu}_{zz}x_6 + \tilde{\mu}_{yz}); \qquad x_3 = -\frac{1}{\lambda_2^x}(\tilde{\mu}_{yz}x_6 + \tilde{\mu}_{yy})$$

(B.5)

Similarly, y_1 through y_6 are temporary variables that are evaluated by the following stack of equations

$$y_6 = \frac{\tilde{\varepsilon}_{zz}\tilde{\mu}_{yz} - \tilde{\varepsilon}_{yz}\tilde{\mu}_{zz}}{2((\lambda_2^x)^2 + \tilde{\varepsilon}_{yz}\tilde{\mu}_{yz} - \tilde{\varepsilon}_{yy}\tilde{\mu}_{zz})};$$
$$y_1 = \frac{1}{\lambda_2^x}(\tilde{\varepsilon}_{xy}y_6 - \tilde{\varepsilon}_{xz}/2); \qquad y_2 = \frac{1}{\lambda_2^x}(\tilde{\varepsilon}_{yy}y_6 - \tilde{\varepsilon}_{yz}/2); \qquad y_3 = \frac{1}{\lambda_2^x}(\tilde{\varepsilon}_{yz}y_6 - \tilde{\varepsilon}_{zz}/2);$$
$$y_4 = \frac{1}{\lambda_2^x}(\tilde{\mu}_{xz}y_2 - \tilde{\mu}_{xy}y_3)$$

(B.6)

The eigenvectors l_5^x and r_5^x are obtained from eqns. (B.4) to (B.6) after setting $l_2^x \to l_5^x$, $r_2^x \to r_5^x$ and $\lambda_2^x \to \lambda_5^x$. The eigenvectors l_6^x and r_6^x are obtained from eqns. (B.1) to (B.3) after setting $l_1^x \to l_6^x$, $r_1^x \to r_6^x$ and $\lambda_1^x \to \lambda_6^x$. Please note that the left and right eigenvectors will not be normalized, but that normalization is easy to accomplish post facto.

The eigenvalues in eqn. (2.16) are so designed that we smoothly retrieve the limit in eqn. (2.14) when the permittivity and permeability become diagonal tensors. We can, therefore, design eigenvectors that smoothly retrieve the eigenvectors in eqns. (A.3) and (A.4). Let l_1^y and r_1^y denote the left and right eigenvectors corresponding to $\lambda_1^y = -\sqrt{\tau^y + \chi^y \sqrt{\kappa^y}}/\sqrt{2}$. I.e., λ_1^y is the first eigenvalue in the diagonal matrix Λ^y, and so on. We formally write l_1^y and r_1^y in a form that could retrieve the eigenvectors in eqns. (A.3) and (A.4) as

$$r_1^y = \begin{pmatrix} x_1, & 0, & x_3, & x_4, & 0, & 1 \end{pmatrix}^T$$
$$l_1^y = \begin{pmatrix} y_1, & y_2, & y_3, & y_4, & y_5, & \frac{1}{2} \end{pmatrix}$$

(B.7)

Here x_1, x_3 and x_4 are temporary variables that are evaluated by the following stack of equations

$$x_4 = \frac{\tilde{\varepsilon}_{zz}\tilde{\mu}_{xz} - \tilde{\varepsilon}_{xz}\tilde{\mu}_{zz}}{(\lambda_1^y)^2 + \tilde{\varepsilon}_{xz}\tilde{\mu}_{xz} - \tilde{\varepsilon}_{zz}\tilde{\mu}_{xx}};$$
$$x_1 = -\frac{1}{\lambda_1^y}(\tilde{\mu}_{xz}x_4 + \tilde{\mu}_{zz}); \qquad x_3 = \frac{1}{\lambda_1^y}(\tilde{\mu}_{xx}x_4 + \tilde{\mu}_{xz})$$

(B.8)

Similarly, y_1 through y_5 are temporary variables that are evaluated by the following stack of equations

$$y_4 = \frac{\tilde{\varepsilon}_{xx}\tilde{\mu}_{xz} - \tilde{\varepsilon}_{xz}\tilde{\mu}_{xx}}{2((\lambda_1^y)^2 + \tilde{\varepsilon}_{xz}\tilde{\mu}_{xz} - \tilde{\varepsilon}_{zz}\tilde{\mu}_{xx})};$$
$$y_1 = \frac{1}{\lambda_1^y}(\tilde{\varepsilon}_{xz}y_4 - \tilde{\varepsilon}_{xx}/2); \qquad y_2 = \frac{1}{\lambda_1^y}(\tilde{\varepsilon}_{yz}y_4 - \tilde{\varepsilon}_{xy}/2); \qquad y_3 = \frac{1}{\lambda_1^y}(\tilde{\varepsilon}_{zz}y_4 - \tilde{\varepsilon}_{xz}/2);$$
$$y_5 = \frac{1}{\lambda_1^y}(\tilde{\mu}_{xy}y_3 - \tilde{\mu}_{yz}y_1)$$

(B.9)

Let l_2^y and r_2^y denote the left and right eigenvectors corresponding to $\lambda_2^y = -\sqrt{\tau^y - \chi^y \sqrt{\kappa^y}}/\sqrt{2}$. We formally write l_2^y and r_2^y in a form that could retrieve the eigenvectors in eqns. (A.3) and (A.4) as

$$r_2^y = \begin{pmatrix} x_1, & 0, & x_3, & 1, & 0, & x_6 \end{pmatrix}^T$$
$$l_2^y = \begin{pmatrix} y_1, & y_2, & y_3, & \frac{1}{2}, & y_5, & y_6 \end{pmatrix}$$

(B.10)

Here x_1, x_3 and x_6 are temporary variables that are evaluated by the following stack of equations

$$x_6 = \frac{\tilde{\varepsilon}_{xx}\tilde{\mu}_{xz} - \tilde{\varepsilon}_{xz}\tilde{\mu}_{xx}}{(\lambda_2^y)^2 + \tilde{\varepsilon}_{xz}\tilde{\mu}_{xz} - \tilde{\varepsilon}_{xx}\tilde{\mu}_{zz}};$$

$$x_1 = -\frac{1}{\lambda_2^y}(\tilde{\mu}_{zz}x_6 + \tilde{\mu}_{xz}); \qquad x_3 = \frac{1}{\lambda_2^y}(\tilde{\mu}_{xz}x_6 + \tilde{\mu}_{xx})$$

(B.11)

Similarly, y_1 through y_6 are temporary variables that are evaluated by the following stack of equations

$$y_6 = \frac{\tilde{\varepsilon}_{zz}\tilde{\mu}_{xz} - \tilde{\varepsilon}_{xz}\tilde{\mu}_{zz}}{2((\lambda_2^y)^2 + \tilde{\varepsilon}_{xz}\tilde{\mu}_{xz} - \tilde{\varepsilon}_{xx}\tilde{\mu}_{zz})};$$

$$y_1 = -\frac{1}{\lambda_2^y}(\tilde{\varepsilon}_{xx}y_6 - \tilde{\varepsilon}_{xz}/2); \qquad y_2 = -\frac{1}{\lambda_2^y}(\tilde{\varepsilon}_{xy}y_6 - \tilde{\varepsilon}_{yz}/2); \qquad y_3 = -\frac{1}{\lambda_2^y}(\tilde{\varepsilon}_{xz}y_6 - \tilde{\varepsilon}_{zz}/2);$$

(B.12)

$$y_5 = \frac{1}{\lambda_2^y}(\tilde{\mu}_{xy}y_3 - \tilde{\mu}_{yz}y_1)$$

The eigenvectors l_5^y and r_5^y are obtained from eqns. (B.10) to (B.12) after setting $l_2^y \rightarrow l_5^y$, $r_2^y \rightarrow r_5^y$ and $\lambda_2^y \rightarrow \lambda_5^y$. The eigenvectors l_6^y and r_6^y are obtained from eqns. (B.7) to (B.9) after setting $l_1^y \rightarrow l_6^y$, $r_1^y \rightarrow r_6^y$ and $\lambda_1^y \rightarrow \lambda_6^y$. Please note that the left and right eigenvectors will not be normalized, but that normalization is easy to accomplish post facto.

Appendix C

Imposing the constraint from eqn. (3.3) now gives us three conditions from the linear terms; they are

$$\frac{2a_{xx}}{\Delta x} + \frac{b_{xy}}{\Delta y} + \frac{c_{xz}}{\Delta z} = \Delta_x\rho_{E;0}; \qquad \frac{a_{xy}}{\Delta x} + \frac{2b_{yy}}{\Delta y} + \frac{c_{yz}}{\Delta z} = \Delta_y\rho_{E;0}; \qquad \frac{a_{xz}}{\Delta x} + \frac{b_{yz}}{\Delta y} + \frac{2c_{zz}}{\Delta z} = \Delta_z\rho_{E;0}$$

(C.1)

The constant term from the constraint equation, eqn. (3.3), gives

$$\frac{a_x}{\Delta x} + \frac{b_y}{\Delta y} + \frac{c_z}{\Delta z} = \bar{\rho}_{E;0}$$

(C.2)

We will soon see that the above equation is equivalent to eqn. (3.1) and provides no new information.

Matching the linearly varying parts of $D^x(x = \pm\Delta x/2, y, z)$ from eqn. (3.7) with the corresponding terms from eqn. (3.4) we get

$$a_y = (\Delta_y D_0^{x+} + \Delta_y D_0^{x-})/2; \qquad a_{xy} = \Delta_y D_0^{x+} - \Delta_y D_0^{x-};$$

$$a_z = (\Delta_z D_0^{x+} + \Delta_z D_0^{x-})/2; \qquad a_{xz} = \Delta_z D_0^{x+} - \Delta_z D_0^{x-}$$

(C.3)

Matching the linearly varying parts of $D^y(x, y = \pm\Delta y/2, z)$ from eqn. (3.8) with the corresponding terms from eqn. (3.5) we get

$$b_x = (\Delta_x D_0^{y+} + \Delta_x D_0^{y-})/2; \qquad b_{xy} = \Delta_x D_0^{y+} - \Delta_x D_0^{y-};$$

$$b_z = (\Delta_z D_0^{y+} + \Delta_z D_0^{y-})/2; \qquad b_{yz} = \Delta_z D_0^{y+} - \Delta_z D_0^{y-}$$

(C.4)

Matching the linearly varying parts of $D^z(x, y, z = \pm\Delta z/2)$ from eqn. (3.9) with the corresponding terms from eqn. (3.6) we get

$$c_x = (\Delta_x D_0^{z+} + \Delta_x D_0^{z-})/2; \qquad c_{xz} = \Delta_x D_0^{z+} - \Delta_x D_0^{z-};$$

$$c_y = (\Delta_y D_0^{z+} + \Delta_y D_0^{z-})/2; \qquad c_{yz} = \Delta_y D_0^{z+} - \Delta_y D_0^{z-}$$

(C.5)

The constraints from eqn. (C.1) can now be used to obtain expressions for a_{xx}, b_{yy} and c_{zz} as follows

$$a_{xx} = \frac{\Delta x}{2}\left(\Delta_x\rho_{E;0} - \frac{b_{xy}}{\Delta y} - \frac{c_{xz}}{\Delta z}\right); \qquad b_{yy} = \frac{\Delta y}{2}\left(\Delta_y\rho_{E;0} - \frac{a_{xy}}{\Delta x} - \frac{c_{yz}}{\Delta z}\right); \qquad c_{zz} = \frac{\Delta z}{2}\left(\Delta_z\rho_{E;0} - \frac{a_{xz}}{\Delta x} - \frac{b_{yz}}{\Delta y}\right)$$

(C.6)

Matching the constant parts of $D^x(x = \pm\Delta x/2, y, z)$ from eqn. (3.7) with the corresponding terms from eqn. (3.4) we get

$$a_x = \bar{D}_0^{x+} - \bar{D}_0^{x-}; \qquad a_0 = (\bar{D}_0^{x+} + \bar{D}_0^{x-})/2 - a_{xx}/6$$

(C.7)

Matching the constant parts of $D^y(x, y = \pm\Delta y/2, z)$ from eqn. (3.8) with the corresponding terms from eqn. (3.5) we get

$$b_y = \bar{D}_0^{y+} - \bar{D}_0^{y-}; \qquad b_0 = (\bar{D}_0^{y+} + \bar{D}_0^{y-})/2 - b_{yy}/6$$

(C.8)

Matching the constant parts of $D^z(x, y, z = \pm\Delta z/2)$ from eqn. (3.9) with the corresponding terms from eqn. (3.6) we get

$$c_z = \bar{D}_0^{z+} - \bar{D}_0^{z-}; \qquad c_0 = (\bar{D}_0^{z+} + \bar{D}_0^{z-})/2 - c_{zz}/6 \tag{C.9}$$

It is best to evaluate eqns. (C.3) to (C.9) in the order that they are listed here. This gives us all the coefficients in eqns. (3.7), (3.8) and (3.9), thereby completing our description of constraint preserving reconstruction. Also notice from the expressions for a_x, b_y and c_z in the previous three equations that eqn. (C.2) will be automatically satisfied because of the definition in eqn. (3.1).

References

[1] D.S. Balsara, D.S. Spicer, A staggered mesh algorithm using high order Godunov fluxes to ensure solenoidal magnetic fields in magnetohydrodynamic simulations, J. Comput. Phys. 149 (1999) 270–292.

[2] D.S. Balsara, Divergence-free adaptive mesh refinement for magnetohydrodynamics, J. Comput. Phys. 174 (2001) 614–648.

[3] D.S. Balsara, Second-order-accurate schemes for magnetohydrodynamics with divergence-free reconstruction, Astrophys. J. Suppl. 151 (2004) 149–184.

[4] D.S. Balsara, Divergence-free reconstruction of magnetic fields and WENO schemes for magnetohydrodynamics, J. Comput. Phys. 228 (2009) 5040–5056.

[5] D.S. Balsara, C.-W. Shu, Monotonicity preserving weighted non-oscillatory schemes with increasingly high order of accuracy, J. Comput. Phys. 160 (2000) 405–452.

[6] D.S. Balsara, T. Rumpf, M. Dumbser, C.-D. Munz, Efficient, high accuracy ADER-WENO schemes for hydrodynamics and divergence-free magnetohydrodynamics, J. Comput. Phys. 228 (2009) 2480–2516.

[7] D.S. Balsara, Multidimensional HLLE Riemann solver; application to Euler and magnetohydrodynamic flows, J. Comput. Phys. 229 (2010) 1970–1993.

[8] D.S. Balsara, A two-dimensional HLLC Riemann solver for conservation laws: application to Euler and magnetohydrodynamic flows, J. Comput. Phys. 231 (2012) 7476–7503.

[9] D.S. Balsara, M. Dumbser, C. Meyer, H. Du, Z. Xu, Efficient implementation of ADER schemes for Euler and magnetohydrodynamic flow on structured meshes – comparison with Runge–Kutta methods, J. Comput. Phys. 235 (2013) 934–969.

[10] D.S. Balsara, M. Dumbser, R. Abgrall, Multidimensional HLL and HLLC Riemann solvers for unstructured meshes – with application to Euler and MHD flows, J. Comput. Phys. 261 (2014) 172–208.

[11] D.S. Balsara, Multidimensional Riemann problem with self-similar internal structure – Part I – Application to hyperbolic conservation laws on structured meshes, J. Comput. Phys. 277 (2014) 163–200.

[12] D.S. Balsara, M. Dumbser, Divergence-free MHD on unstructured meshes using high order finite volume schemes based on multidimensional Riemann solvers, J. Comput. Phys. 299 (2015) 687–715.

[13] D.S. Balsara, M. Dumbser, Multidimensional Riemann problem with self-similar internal structure – Part II – Application to hyperbolic conservation laws on unstructured meshes, J. Comput. Phys. 287 (2015) 269–292.

[14] D.S. Balsara, Three dimensional HLL Riemann solver for structured meshes; application to Euler and MHD flow, J. Comput. Phys. 295 (2015) 1–23.

[15] D.S. Balsara, J. Vides, K. Gurski, B. Nkonga, M. Dumbser, S. Garain, E. Audit, A two-dimensional Riemann solver with self-similar sub-structure – alternative formulation based on least squares projection, J. Comput. Phys. 304 (2016) 138–161.

[16] D.S. Balsara, T. Amano, S. Garain, J. Kim, High order accuracy divergence-free scheme for the electrodynamics of relativistic plasmas with multidimensional Riemann solvers, J. Comput. Phys. 318 (2016) 169–200.

[17] D.S. Balsara, S. Garain, C.-W. Shu, An efficient class of WENO schemes with adaptive order, J. Comput. Phys. 326 (2016) 780–804.

[18] D.S. Balsara, R. Käppeli, Von Neumann stability analysis of globally divergence-free RKDG and PNPM schemes for the induction equation using multidimensional Riemann solvers, J. Comput. Phys. 336 (2017) 104–127.

[19] A. Barbas, P. Velarde, Development of a Godunov method for Maxwell's equations with adaptive mesh refinement, J. Comput. Phys. 300 (2016) 186–201.

[20] J.-P. Berenger, A perfectly matched layer for the absorption of electromagnetic waves, J. Comput. Phys. 114 (2) (1994) 185–200.

[21] J.-P. Berenger, Three-dimensional perfectly matched layer for the absorption of electromagnetic waves, J. Comput. Phys. 127 (2) (1996) 363–379.

[22] S.H. Brecht, J.G. Lyon, J.A. Fedder, K. Hain, A simulation study of east–west IMF effects on the magnetosphere, Geophys. Res. Lett. 8 (1981) 397.

[23] S.H. Chang, A. Taflove, Finite-difference time-domain model of lasing action in a four-level two-electron system, Opt. Express 12 (2004) 3827–3833.

[24] W. Dai, P.R. Woodward, On the divergence-free condition and conservation laws in numerical simulations for supersonic magnetohydrodynamic flows, Astrophys. J. 494 (1998) 317–335.

[25] C.R. DeVore, Flux-corrected transport techniques for multidimensional compressible magnetohydrodynamics, J. Comput. Phys. 92 (1991) 142–160.

[26] M. Dumbser, M. Käser, Arbitrary high order non-oscillatory finite volume schemes on unstructured meshes for linear hyperbolic systems, J. Comput. Phys. 221 (2007) 693–723.

[27] M. Dumbser, D. Balsara, E.F. Toro, C.D. Munz, A unified framework for the construction of one-step finite volume and discontinuous Galerkin schemes on unstructured meshes, J. Comput. Phys. 227 (2008) 8209–8253.

[28] M. Dumbser, O. Zanotti, A. Hidalgo, D.S. Balsara, ADER-WENO finite volume schemes with space–time adaptive mesh refinement, J. Comput. Phys. 248 (2013) 257–286.

[29] N. Elkina, H. Ruhl, Reflection-free finite volume Maxwell solver for adaptive meshes, J. Comput. Phys. (2017), in press.

[30] C.R. Evans, J.F. Hawley, Simulation of magnetohydrodynamic flows: a constrained transport method, Astrophys. J. 332 (1989) 659.

[31] A. Farjadpour, D. Roundy, A. Rodriguez, M. Ibanescu, P. Bernel, J. Joannopoulos, S. Johnson, P. Burr, Opt. Lett. 31 (2006) 2972–2974.

[32] J. Hesthaven, T. Warburton, Nodal high-order methods on unstructured grids: I. Time-domain solution of Maxwell's equations, J. Comput. Phys. 181 (2002) 186–221.

[33] W. Hundsdorfer, S.J. Ruuth, IMEX extensions of linear multistep methods with general monotonicity and boundedness properties, J. Comput. Phys. 225 (2007) 2016–2042.

[34] T.Z. Ismagilov, Second order finite volume scheme for Maxwell's equations with discontinuous electromagnetic properties on unstructured meshes, J. Comput. Phys. 282 (2015) 33–42.

[35] G.-S. Jiang, C.-W. Shu, Efficient implementation of weighted ENO schemes, J. Comput. Phys. 126 (1996) 202–228.

[36] D.S. Katz, E.T. Thiel, A. Taflove, Validation and extension to three dimensions of the Berenger PML absorbing boundary condition for FD-TD meshes, IEEE Microw. Guided Wave Lett. 4 (8) (1994) 268.

[37] F. Kupka, N. Happenhofer, I. Higueras, O. Koch, Total-variation-diminishing implicit–explicit Runge–Kutta methods for the simulation of double-diffusive convection in astrophysics, J. Comput. Phys. 231 (2012) 3561–3586.

[38] C.-D. Munz, P. Omnes, R. Schneider, E. Sonnendrücker, U. Voß, Divergence correction techniques for Maxwell solvers based on a hyperbolic model, J. Comput. Phys. 161 (2000) 484.

[39] A. Oskooi, C. Kottke, S. Johnson, Opt. Lett. 34 (2009) 2778–2780.

[40] L. Pareschi, G. Russo, Implicit–explicit Runge–Kutta schemes and applications to hyperbolic systems with relaxation, J. Sci. Comput. 25 (2005) 129.

[41] D. Ryu, F. Miniati, T.W. Jones, A. Frank, A divergence-free upwind code for multidimensional magnetohydrodynamic flows, Astrophys. J. 509 (1998) 244–255.

[42] R.J. Spiteri, S.J. Ruuth, A new class of optimal high-order strong-stability-preserving time-stepping schemes, SIAM J. Numer. Anal. 40 (2002) 469–491.

[43] R.J. Spiteri, S.J. Ruuth, Non-linear evolution using optimal fourth-order strong-stability-preserving Runge–Kutta methods, Math. Comput. Simul. 62 (2003) 125–135.

[44] C.-W. Shu, S.J. Osher, Efficient implementation of essentially non-oscillatory shock capturing schemes, J. Comput. Phys. 77 (1988) 439–471.

[45] C.-W. Shu, S.J. Osher, Efficient implementation of essentially non-oscillatory shock capturing schemes II, J. Comput. Phys. 83 (1989) 32–78.

[46] C.-W. Shu, Total variation-diminishing time discretizations, SIAM J. Sci. Stat. Comput. 9 (1988) 1073–1084.

[47] A. Taflove, Review of the formulation and applications of the finite-difference time-domain method for numerical modeling of electromagnetic wave interactions with arbitrary structures, Wave Motion 10 (1988) 547–582.

[48] A. Taflove, S. Hagness, Computational Electrodynamics, third edition, Artech House, 2005.

[49] A. Taflove, A. Oskooi, S. Johnson, Advances in FDTD Computational Electrodynamics – Photonics and Nanotechnology, Artech House, 2013.

[50] A. Taflove, S. Hagness, Finite difference time domain solution of Maxwell's equations, WEEEE Rev. (2016) 8303.

[51] V.A. Titarev, E.F. Toro, ADER: arbitrary high order Godunov approach, J. Sci. Comput. 17 (1–4) (2002) 609–618.

[52] V.A. Titarev, E.F. Toro, ADER schemes for three-dimensional nonlinear hyperbolic systems, J. Comput. Phys. 204 (2005) 715–736.

[53] E.F. Toro, R.C. Millington, R.C.M. Nejad, Towards very high-order Godunov schemes Godunov methods: theory and applications, in: E.F. Toro (Ed.), Edited Review, Kluwer Academic/Plenum Publishers, 2001, pp. 905–937.

[54] E.F. Toro, V.A. Titarev, Solution of the generalized Riemann problem for advection reaction equations, Proc. R. Soc. Lond. Ser. A 458 (2002) 271–281.

[55] B. van Leer, Towards the ultimate conservative difference scheme. IV. A new approach to numerical convection, J. Comput. Phys. 23 (1977) 276–299.

[56] B. van Leer, Towards the ultimate conservative difference scheme V. A second order sequel to Godunov's method, J. Comput. Phys. 32 (1979) 101–136.

[57] K.S. Yee, Numerical solution of initial boundary value problems involving Maxwell equation in an isotropic media, IEEE Trans. Antennas Propag. 14 (1966) 302.

[58] Z. Xu, D.S. Balsara, H. Du, Divergence-free WENO reconstruction-based finite volume scheme for ideal MHD equations on triangular meshes, Commun. Comput. Phys. 19 (04) (2016) 841–880.

[59] A.R. Zakharian, M. Brio, C. Dineen, J.V. Moloney, Second-order accurate FDTD space and time grid refinement method in three space dimensions, IEEE Photonics Technol. Lett. 18 (11) (2006) 1237.